Alumina-Graphene Nanoplatelet Coatings
Using Aerosol Deposition Technique

Hafez Namaki Araghi

A Thesis

In the Department of

Mechanical, Industrial and Aerospace Engineering

Presented in Partial Fulfillment of the Requirements

For the Degree of

Master of Applied Science (Mechanical Engineering)

at Concordia University

Montreal, Quebec, Canada

January 2023

This is to certify that the thesis prepared

By: Hafez Namaki Araghi

Entitled: Alumina-Graphene Nanoplatelet Coatings Using Aerosol Deposition Technique

And submitted in partial fulfilment of the requirements for the degree of

Master of Applied Science (Mechanical Engineering)

Complies with the regulations of the University and meets the accepted standards with respect to originality and quality.

Signed by the final Examining Committee:

_____ Chair

Dr. Moussa.Tembely

_____ External Examiner

Dr. Pantcho Stoyanov

_____ External to Program

_____ Examiner

Dr. Moussa.Tembely

_____ Examiner

_____ Thesis Co-Supervisor

Dr. Martin Pugh

_____ Thesis Co-Supervisor

Dr. Christian Moreau

_____ Thesis Co-Supervisor

Dr. Ali Dolatabadi

Approved by: _____

           Dr. Martin Pugh (Chair of Department)

_____ 2023   _____ Dean of Faculty

           Dr. Mourad Debbabi

Abstract

Alumina-Graphene Nanoplatele Coatings
Using Aerosol Deposition Technique

Hafez Namaki Araghi

Aerosol Deposition (AD) is a novel deposition process for solid-state material deposition at ambient temperature. AD is an excellent candidate for producing ceramic composite coatings due to the even distribution of reinforcing material inside the ceramic matrix.

In this work, AD has been used to create an alumina coating containing 2 weight-percent graphene nanoplatelets (GNPs). In order to prepare this composite powder, alumina and GNPs were milled in cyclohexane by high-energy milling. This powder was then used as the feedstock for aerosol deposition using an in-house vacuum apparatus. Various relevant characteristics, such as stand-off distance, carrier gas, particle size distribution, and nozzle shape, have been examined in order to obtain the operating condition for generating coatings. Successful coatings were achieved on stainless steel substrates for both alumina and alumina-GNP powders after modifying several of the spray parameters.

Studies using Raman spectroscopy have shown that the presence of GNPs in composite feedstock is significant. The coefficient of friction of the composite coatings and pure alumina deposits have both been measured using the micro scratch adhesion test. In tests of micro scratch adhesion with forces ranging from 0.3 to 30 N, it was discovered that the coefficient of friction of the alumina/GNP composite was lower than that of the comparable pure alumina covering. The test findings show that, in comparison to pure alumina deposition, the coefficient of friction in the alumina + GNP coating was reduced by the exfoliation of graphene layers from GNPs. The alumina coating experienced brittle spalling and delamination of the coating from the substrate at the interface, whereas the alumina + GNP coating showed no evidence of adhesion failure. The transition to the serious wear regime occurred between 5.7 and 30 N in progressive load scratch testing for the pure alumina coating, while the initial yield point of the alumina + GNP coating was observed at 7.5 N.SEM was used to characterize the microstructure of this graphene/alumina film.

Acknowledgement

My sincere gratitude and appreciation to my supervisors, Professor Ali Dolatabadi, Professor Christian Moreau and Professor Martin Pugh for their guidance, patience, enthusiasm and their scientific advice in all the time of research.

Very special thanks to Professor Ludvik Martinu from Polytechnique Montreal University for giving me permission to use his research facilities in his laboratories.

Thanks also to my friends and colleagues for their support and encouragement throughout the hard times of my study.

My heartfelt thanks goes to my wife, Mahshid, for their unwavering love and support throughout every stage of my life; I would also want to thank my family for their support. They have been my closest friends and mentors, and my love, respect, and thanks cannot be adequately expressed in words.

I wish to thank the entire Concordia University Thermal Spray Laboratory group members for all the help and encouragement during my work. Special thanks to Dr. Fadhel Ben Ettouil, Dr. Ali Akbar Nozzari and Dr. Navid Sharifi for all the technical help during my experimental work. I would like also appreciate Tahmineh for their support during these challenging period. Thank you for being such a great and helpful team.

Table of Contents

List of Figures

VIII

List of Tables

List of Abbreviations

Abbreviation	Meaning
AD	Aerosol Deposition
AcD	Aerosol co-Deposition
ASI	Adiabatic Shear Instability
CLSM	Confocal Laser Scanning Microscopy
CS	Cold Spray
CVD	Chemical Vapor Deposition
COF	Coefficient of Friction
GNP	Graphene Nanoplatelets
GNR	Graphene Nanoribbons
GO	Graphene Oxide
HA	Hydroxyapatite
HVOF	High-Velocity Oxygen Fuel
L_c	Critical Scratch Load
RTIC	Room Temperature Impact Consolidation
SPS	Spark Plasma Sintering
SOD	Stand-off Distance
SEM	Scanning Electron Microscopy
VCS	Vacuum Cold Spray

List of Symbols

Symbol	Meaning
D_{10}	10% of particles are smaller this particle size
D_{50}	50% of particles are smaller this particle size
D_{90}	90% of particles are smaller this particle size
D_h	Hydraulic diameter
D	Crystallite size
R_a	Arithmetic mean height of the surface on a line
R_z	Maximum height of the surface on a line
S_a	Average surface area
β	Full width at half maximum peak
θ	Peak angle
λ	Wavelength
δ	Dislocation density
κ	Shape factor
I_D/I_G	The ratio of D and G band intensities

Chapter 1.   Introduction

1.1.   Background and Motivation

Aerosol Deposition (AD) has become known as one of the new deposition methods used forsolid state deposition of materials at ambient temperature. In this method, ultrafine particles are propelled through a nozzle with a high-speed gas flow and impact onto a substrate in a chamber under low vacuum level. The particles form a dense coating due to plastic deformation of the particles after impact with the substrate. Inside the nozzle, particles are accelerated to reach a critical velocity.

In the fabrication of ceramic coatings, high temperaturesoften above 1000°C,are usually required.When a significant difference exists between the melting point of the coating material and the substrate, for instance when depositing ceramics on metal or polymer substrates, forming dense coatingswithout damaging or changing the microstructure of the substrate can be difficult.The AD method has been utilized as a recent solution for depositing dense ceramic coatings without high temperatures in the deposition chamber and with raw powder materials on key material substrates.

The historical perspective of this method could be referred back to 1900 when Thurston produced a coating of metallic particles on a substrate by using pressurized gas[1]. After that, in 1958, Rocheville disclosed a device that included Thurston's patent and a de Laval nozzle and deposited fine particles on substrate with higher velocity. In the 1980s, a gas deposition method which consisted of an evaporation and aerosol generation system in order to produce ceramic and metallic coating was made[2].In 1999, Akedo and Lebedev[3], modified the cold gas dynamic spray method for fabricating thick ceramic films. This method, that was named as Aerosol Deposition (AD) or Vacuum Cold Spray (VCS) contains an aerosol generator system and a vacuum chamber. Similar to several coating methods based on solid state collision principles, aerosol flow is

generated by mixing fine particles with a carrier gas and is controlled by gas flow. A low vacuum pressure creates the acceleration and flow of the ceramic particles.

Since 1999, research on the AD process has increased significantly. The potential of the AD process tofabricateceramic coatings on a broad range of materialshas shown applications of this method for fabrication of various thin films in different products including piezoelectric devices, solar cells, solid oxide fuel cell, artificial bone, microwave devices such as chip inductors and in modifying films for abrasion resistance in infrared sensors [4][5].

A variety of ceramic materials have been investigated by the AD method: the most popular being Alumina, TiO2, and lead zirconate titanate (PZT). The AD method also provides an opportunity to produce composite coatings. The gooddistribution of reinforcement material inside the matrix makes AD a very good candidate for fabricating ceramic composite coatings. Due to the low operating temperature of the AD method, phase change of the α-Alumina phase, which can occur in high temperature processesdoes not happen.Dense composite thin film coatings have been obtained through powders mixed in different ratioscomprising ceramic, metallic[6] or polymer[7] components. This process, which is also named as Aerosol co-Deposition (AcD) has been implemented to tailor the properties of composite coatings such asconductivity, permittivity as well as the mechanical properties of deposited films.

Several studies have proposed the AcD method for fabrication of composite coatings. In Kim et al.[8]BaTiO$_3$-PTFEwas produced by AcD to attain a coating with high permittivity. In gas sensor applications, bismuth vanadate and its related components have been investigated by Exner et al.[9] in order to study the behavior of mixing materials with different hardnesses by AcD and analyzing the crack and delamination behaviour of the films.

In an effort to fabricatea dense and thick coating, AcD method has been employed to improve ferroelectric coatings[10]. According to this study, they added lead zinc niobate (PZN) to (PZT) which enhanced the ferroelectric and piezoelectric responses in comparison to a coating comprised only of PZT fabricated by AD.

Graphene-titanium oxide [11], SiC-MoSi$_2$[12], strontium-doped lanthanum manganite (LSM) and yttria stabilized zirconia (YSZ) [13], TiO$_2$with tricalcium phosphate (TCP)[14], NiO and Mn$_2$O$_3$ composite film [15], Cu-TiO$_2$[16]and Au-PZT thin film [17] are some examples of composite coating which have been obtained by AcD.

Among ceramic materials, alumina has outstanding properties in chemical, electrical and mechanical aspects and has been identified as an interesting candidate in coating studies especially as it is relatively low cost. Although its high hardness, chemical inertness, electrical and thermal insulation properties are advantageous in a variety of coatings, brittleness andlow fracture toughness restrict its application. Therefore, many efforts have been taken to overcome these weaknesses.

In one of the first attempts, Akedo et al. [18]made a composite coating of Al_2O_3 and PZT to estimate the effect of powder mix on coating consolidation in the AD process. To improve electrical properties, adding alumina to polymers materials has been also investigated. In these studies, the effect of alumina on the mechanical properties of the composite coating [7] or surface topography of deposition [19] were studied.

Over the last decade, graphene nanoplatelets (GPN) and graphite have been utilized to obtain higher mechanical and electrical properties in ceramic composites. Graphene nanoplatelets are promising for reinforcement of alumina composites where the graphene is well-dispersed in the matrix. By serving as a filler to deflect the propagation of a crack, graphene platelets enhance fracture toughness. Additionally, the dispersion of graphene near the grain boundary assists in transferring load away from the matrix grain.[20]. Review of the literature reveals a lack of study on the application of AD for alumina-graphene nanoplatelet (GNP) composite coatings thus it would seem appropriate to try this approach. The common issues of thermal spray techniques along with opportunities in obtaining dense and compressed composite coating with the AD method were among the motivation factors for this study. This research thesis provides an investigative framework for preparing composite powders, creating the coating and analyzing the given results.

1.2.   Objectives

This study aims to investigate AD methods as an alternative process to produce a composite coating of alumina-graphene. The main advantages of proposing this novel method include:

- Fully dense film deposition with low porosity
- Good coating adhesion
- Prevent the substrate's transformation during spraying.
- Obtaining a desirable -alumina crystal structure in the film coating
- Dispersion of graphene/graphene nanoplatelet inside the ceramic matrix
- Avoiding phase transformation of the substrate

The research objectives are as follow:

- Identify the effect of particle size and pretreatment of mixing powder on the quality and the rate of deposition
- Explore the effect of different deposition parameters in order to achieve a dense and well-adhered coating
- Investigate to what extent graphene additions influence the wear behavior (e.g. friction coefficient) of the composite coating

1.3.   Thesis Outline

This work was performed with the goal of fabricating alumina-graphene nanoplatelet coatings for applications in wear resistance using AD. This thesis is dividedinto five chapters. A brief description of the chapters are as follows:

Chapter 1 discusses the background and motivation of this research thesis. The objectives and the scope of work are also explained.

Chapter 2 reviews the literature starting with describing the aerosol deposition setup followed by discussion of the mechanism of layer fabrication. Section 2.3 explores the application of graphene-alumina based coatings, followed by summary discussion of previous research on this topic. In Chapter 3, the experimental part of the work is detailed. Chapter 4 presents and discusses the thesis results. Coating characterization and the data obtained are presented, and further observations are performed. As a final point, the conclusions of the work and future research are specified in Chapter 5.

Chapter 2.   Literature Review

This chapter will describe the AD system, the proposed mechanisms of bonding upon impingement of particles and some applications of graphene composite coatings. Additionally, graphene-based coatings from other spraying methods will be compared. Finally, various coating procedures will be explained.

2.1.   The AD process

The main setup of AD consists of two air-tight chambers that are connected to each other; the first one is an aerosol generation chamber that produces the aerosol which is then transferred and deposited in the deposition chamber. The aerosol generation chamber is attached to a carrier gas cylinder and a vibration system to combine the powder with the carrier gas. The second chamber is the deposition chamber that is used for formation of the film. The deposition chamber consists of a nozzle and a substrate holder. A rotary vacuum pump and a booster pump is connected to the vacuum chamber in order to generate low pressure (about 1 Torr) inside the deposition chamber. The vacuum pressure is measured by gages that are connected to the deposition chamber (P_{DC}) and booster pump (P_H) (Figure 2-1).

Inside the aerosol generation chamber, the carrier gas feeds into a fluidized bed of the particles through gas injection nozzles. The carrier gas picks up the dried micro-particles and creates a vortex flow of the aerosol. In the bottom of the aerosol chamber a diaphragm plate is vibrating to keep particles moving into the gas flow. Fluidized bed vibration can also be used in conjunction with the carrier gas to carry out individual particles to the entrance of the nozzle for spraying. The pressure difference between the two chambers drives the aerosol particles to move from the aerosol chamber through a nozzle to the vacuum deposition chamber. The particles are accelerated to a high velocity and ejected through the nozzle into the deposition chamber and onto the substrate to be coated. The accelerated aerosol in the converging or converging-diverging (de Laval) type

nozzle forms an aerosol jet with velocities between 100 and 600 m/s, at its outlet. These high speed particles breakup into nano-sized particles when colliding into the substrate and re-bond to form the dense ceramic film [21].
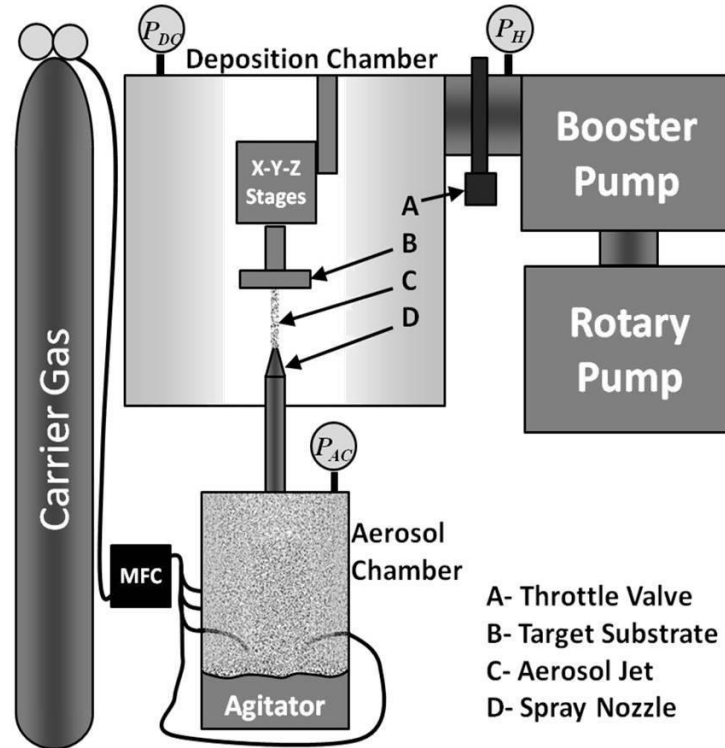
Figure 2-1:The main components of AD. The pressure inside the vacuum chamber and pump head are detected by P_{DC} and P_H, respectively [22].

During impact, depending on the size and critical velocity of the particles, different deposition patterns can be observed. A successful AD coating depends on the following parameters: particle size, carrier gas, flow rate, stand-off distance and scan speed. Compressed air[4], N_2[23], O_2[24], Ar[25]and He[26] have been used as the carrier gas. The range of gas flow rate has been changed from 0.5 to 30 l/min. In addition, stand-off distances between 0.5mm and 50 mm have been reported in the literatures[4]. Film thickness also depends on the scan speed of the substrate in front of the nozzle.

The mechanism of bonding in AD have not been clarified precisely. Some studies attempted to explain the formation of bonding between particle-particle and particle-substrate interfaces based on the particle's kinetic energy, plastic deformation and grain size fragmentation but more work is needed to achieve a full understanding of this phenomenon. In the next section, a summary of previous studies of particle bonding mechanisms is presented.

2.2.   Deposition mechanism of AD

In some ways, AD is comparable with Cold Spray (CS) in which metallic particles are accelerated to supersonic velocities by pressurized gas. In CS, Adiabatic Shear Instability (ASI) and Plastic Flow Localization have been defined as dominant mechanisms in the creation of coatings[27]. Under adiabatic conditions, plastic strain energy is dissipated as heat which causes material softening. Adiabatic softening in association with relatively high contact pressure promotes the formation of the coating via plastic deformation at the particle/substrate contacting surface. Thus, once the conditions for the onset of adiabatic shear localization and adiabatic softening are reached at sufficiently high impact particle velocities (as in CS), the conditions for extensive adhesion of the particle and substrate surfaces are reached resulting in particle/substrate bonding. Schematic stress-strain curves in a normal strain-hardening, adiabatic shear localization and adiabatic softening are shown in Figure2-2 [28].
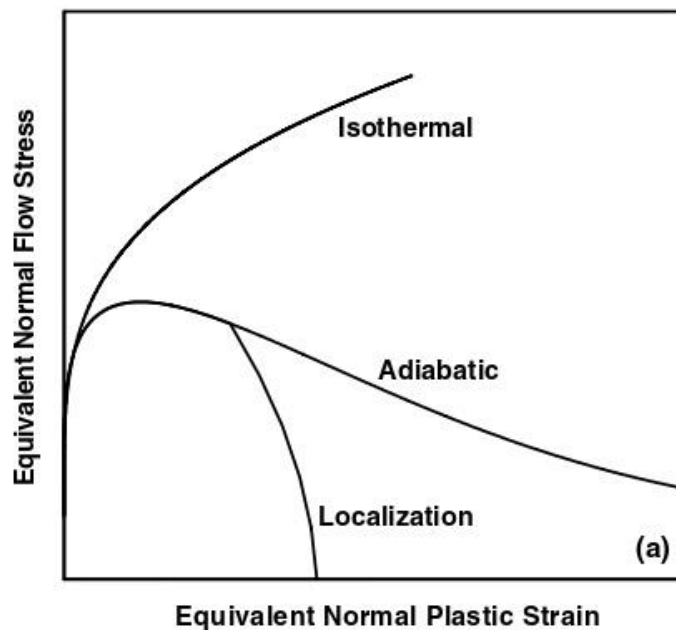
Figure 2-2:Comparison between typical normal stress-strain (Isothermal), adiabatic softening (Adiabatic) and adiabatic shear localization (Localization) curves [28].

In AD, particle deposition is likely different from that for CS metal. Bonding mechanisms for brittle materials on impingement with the substrate is correlated to crack propagation and fragmentation under high velocity impact. In addition, the speed and average size of colliding

particles are different in AD to CS. The particle size and state of agglomeration also cause different deposition patterns in AD[4] .

When a supersonic flow leaves a nozzle and strikes a substrate, like in the AD process, a stagnation zone or bubble occurs. This contributes to the production of a bow shock. A bow shock is produced when gas particles collide with the surface of the substrate, causing a shift in momentum and energy. This quick transfer of energy generates microscopic pressure waves that condense at the surface to produce a normal shock. This shock is intercepted by the incoming flow, resulting in a radial deflection. If the substrate is positioned perpendicular to the exit nozzle, the resulting deflection exceeds the maximum angle of deflection permitted by oblique shock waves. This produces a detachable, curved shockwave known as a bow shock. This shock has a substantial effect on the incoming flow because it acts as an unwelcome barrier to the substrate, slowing and deflecting the particles, hence reducing deposition efficiency.

Smaller particles attain higher velocities than bigger particles in the free-jet condition, however when small particles, less than 100 nm in diameter, are exposed to the substrate, they are decelerated and deflected before impacting and might bounce off the surface owing to the impact of the substrate, stagnation flow, and bow shock. On the other hand, particles that are 200nm – 2μm in size, create a more adhesive and dense coating as the variability of particle size provides sufficient particle kinetic energy and promotes the impact and adhering of particles to the substrate. Although this range of particle sizes provides the optimum particle kinetic energy, deposition still depends on other physical properties of particles such as hardness and fracture toughness of materials.

Larger particles, more than 10 μm, can achieve higher velocity upon impact and less deviation. Consequently, this higher kinetic energy can lead to surface erosion or an abrasion of the film coating. Furthermore, the degree of agglomeration has a considerable impact on the process. In the case of agglomerated particles, kinetic energy induces deagglomeration rather than adhesion, resulting in a porous coating with poor adhesive strength. Effect of particle size on deposition condition is presented in Figure 2-3 [4].

Depending on the particle size, deformation of a ceramic materialcan change from brittle to ductile deformation. Sarobol et al. described the role of nucleation/motion of dislocations on plastic deformation of alumina submicron particles (for particle diameters between 0.3μmand 3.0μm)[29].Kuroyanagi et al. conducted an in situ compression test for a single alumina particle

with a wide particle size ranging from 0.14μm to 32μm to address the occurrence of the brittle to ductile transition (BDT). This study revealed that the fracture occurs by crack penetration. In small particles, the chance of the existence of large defects as the initiation point for fracture, is reduced. Therefore, the required stress for crack propagation becomes larger. As a consequence, the brittle materials can exhibit plasticity or ductile behavior under a certain condition, especially at the fine size scale[29].

The evidence of plastic deformation for single crystal alumina particle shows the plastic deformation has been obtained in defect-free 0.3 μm particles with relatively large strain before fragmentation, while 3 μm particle fractured into many pieces in a brittle way under compression loading. In small particles, dislocation activity was observed [30].
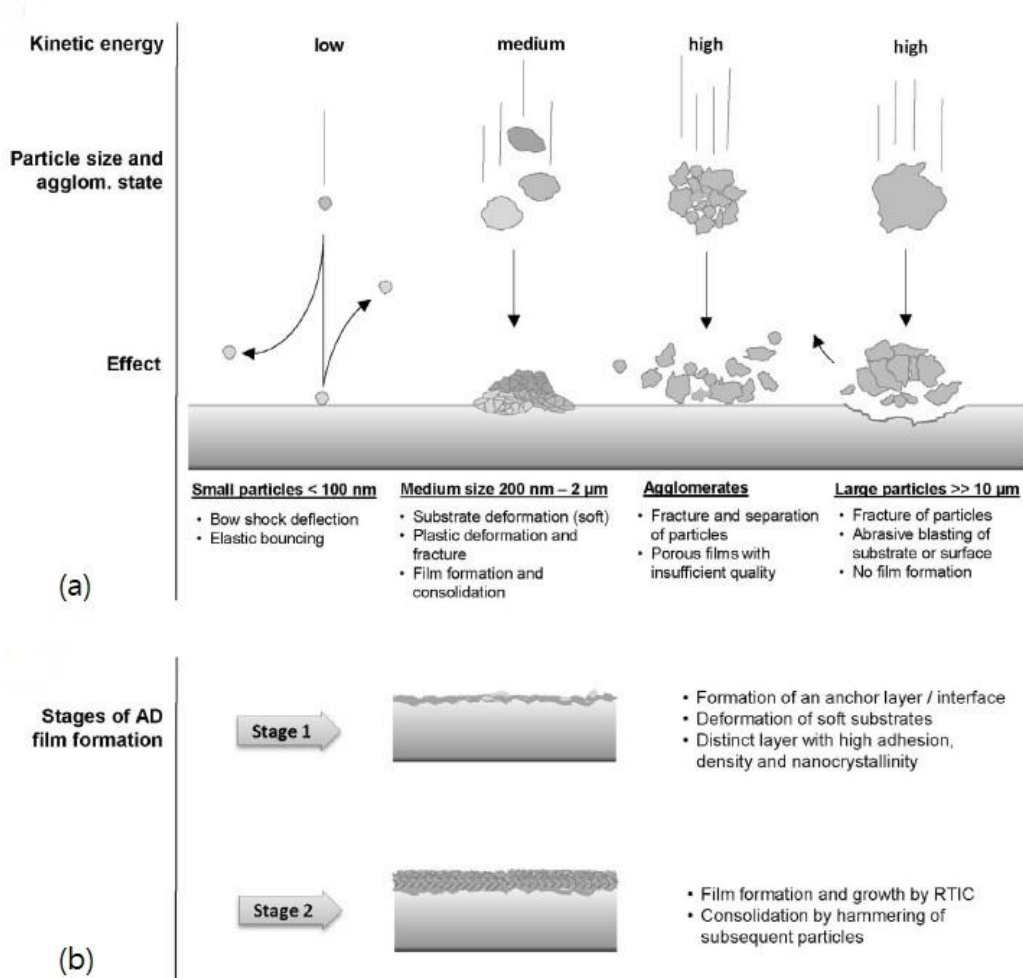
Figure 2-3: (a)Typical configuration of particle-substrate collision and influence of size and kinetic energy of particle. (b)Process of generating anchor layers and building up the coating film [4].

In addition, mechano-chemical phenomena have been reported as the driving mechanism for ceramic deposition through changing the phase of the material by converting the mechanical or kinetic energy to chemical energy. Iwata et al. reported phase transformation in deposition of AlN due to AD. In the deposition film, some part of the hexagonal structure (wurtzite) transformed into the cubic structure (rock salt) which is stable only at high pressure. The high kinetic energy of the accelerated particle could be dissipated by heat causing the phase transformation [31].

Akedo indicates that the film formation in the AD process mainly consists of the fabrication of an anchor layer, and building up the film through subsequent impacts. The primary impacting particles create an initial plastic deformation on the substrate surface and enhance its roughness in the first stage (Stage 1 in Figure 2-3). Crack propagation occurs followed by fragmentation of particles that collide with the substrate. Due to the high velocity impact, a new chemically active surface is formed on the crushed particles. As a result, fine fragmented particles bond due to the collision pressure. Movement and rotation allow for local fragment arrangement and densification.

Film growth occurs in the consolidation stage with reduction of crystallite size and deformation of impacted particles in the deposited layers. The atomic scale contact in the fresh, activated surfaces of the embedded particles (which are also in the vacuum chamber) allows them to recombine, bonding with incoming particles at the interfaces. This process, which includes the plastic deformation and grain size fragmentation, has been called Room Temperature Impact Consolidation (RTIC) [5][22].

The sequence of particle fragmentation and consolidation to final formation is indicated in Figure 2-4.
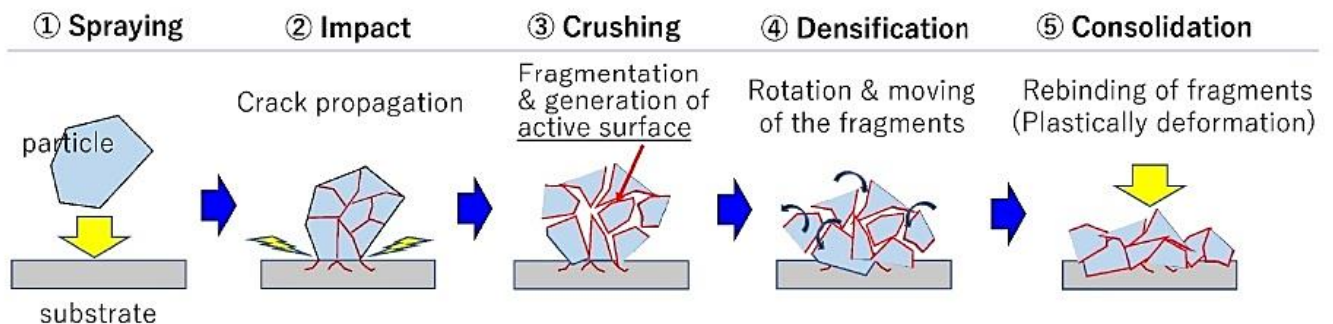
Figure 2-4: Schematic of ceramic fine particle impingement and film formation in AD [22].

From the perspective of deposition mechanism, Akedo indicates the brittle to ductile transition for ceramic material occurs at room temperature depending on the particle diameter. He declared, under the high pressure of impact, plastic flow occurs for sub-micron ceramic particles at room temperature, and new surfaces are formed on the particle surface. As a result, dense, highly transparent ceramic films can be obtained at room temperature [22].

2.3. Graphene-Alumina composites as coating

Alumina has been widely used in different industrial products because of its outstanding properties such as relatively high hardness, chemical inertness, electrical and thermal insulation. In this context, high speed cutting tools [32], dental implants [33], chemical and electrical insulators [34][35], wear resistance parts[36] are some examples. However, alumina is categorized as a brittle material with low fracture toughness, restricting its applications.

In order to overcome this issue, adding reinforcing material into the matrix as a second phase has been suggested. Over the last decade, graphene has been utilized to obtain higher mechanical and electrical properties in ceramic composites. The graphene consists of carbon in a honeycomb crystal lattice which is formed from the 3σ bonds in 2px, 2py and 2s orbitals. On one hand, these σ covalent bonds provide the excellent mechanical properties of graphene. On the other hand, two adjacent atoms through the 2pz orbitals form a π band increasing the charge carrier mobility. This special crystal structure exhibits excellent electrical conductivity, and relatively high Young's modulus[37]. These unique characteristics makes graphene an attractive material to be added to ceramic oxides including alumina [20],[37–42]. These cited studies targeted alumina-based composites reinforced with graphene, fabricated by Spark Plasma Sintering (SPS), and investigated the effect of graphene content on flexural strength, fracture toughness, wear behavior and electrical conductivity.

Graphene is a promising material to reinforce alumina composites where graphene is well-dispersed in the matrix. The graphene sheets which are embedded between the grains, will be anchored to the matrix grains. Therefore, it will increase crack deflection in the contact area between graphene sheets and alumina grains. It will correspondingly improve the fracture toughness of the alumina matrix. Graphene platelets also act as filler to deflect crack propagation; the more deflection, the more stress release and the more increase in fracture toughness.

Furthermore, the distribution of graphene in the grain boundary contributes to transferring the load from the matrix grain which results in improving the mechanical properties of composite [20].

Graphene alumina composites have also been employed in film coating applications mostly including corrosion resistance[40],[43] and wear performance [44–46]. When it comes to corrosion resistance, alumina-based composite coating with graphene exhibits significant improvement as reported by [40], [43]. Amudha et al. [43] employed Atmospheric Plasma Spray (APS) technique for depositing the composite coating. They analyzed to what extent the enhanced corrosion resistance can vary depending on weight percent of graphene oxide inside the alumina composite coating. It was concluded that 1.5wt% of graphene oxide addition provided a significant improvement in surface corrosion resistance. In another study, Mondal et al.[40] laminated composite layers of Al_2O_3 and TiO_2 with graphene oxide and investigated its effect on corrosion resistance compared to individual graphene oxide layer. They revealed that in a salt solution environment, the composite coating is more resistant in the long-term. No damage was observed after 30 days in the corrosive environment.

Prior studies showed that when graphene is coated with alumina, it is noteworthy that the composite provides better wear resistance as well [44][45]. The recent study by Murray et al. [44]employed the spray method of high velocity oxy-fuel (HVOF) to compare the wear rates of alumina based-1%wt graphene and pure alumina. The results displayed a considerable reduction in the wear rate for the composite coating.

Wang et al. [45] fabricated a composite coating of Al_2O_3-TiO_2 by means of plasma spray technique. Graphene in different mass ratios, between 3% and 12%, were mixed to the starting feedstock. It was revealed that 6% addition of graphene resulted in the lowest porosity number and wear rate. More specifically, in the best situation, the porosity number and wear rate of the coating were reduced by 35% and 25% respectively.

The main issue in the application of thermal spraying methods for fabrication of alumina composite coatings centers around controlling the α-phase of the alumina at high temperature [47], [48]. Additionally, the efficiency of the composite film is related to how well graphene is distributed inside the matrix structure. This quality cannot be reached straightforwardly by thermal spray methods. The advanced methods of CS and AD are less sensitive to these issues as supported by the findings of Wang et al. [49] for alumina graphene using CS, Kim et al. [11] for TiO_2-Graphene and Liu et al. [50] for Hydroxyapatite/Graphene using AD.

AD produces dense and well-adhering thin-films directly at room temperature and low pressure, without requiring any heating or sintering of the ceramic [21].

To the best of the author's knowledge, there are only two studies with a focus on the application of graphene in composite coatings by means of the AD method. Lie et al. [50] deposited hydroxyapatite (HA)-graphene composite coating on a titanium substrate. This composite coating showed significant improvements in fracture toughness compared to the pure HA film. Moreover, HA-1wt% of graphene exhibited a remarkable increase in elastic module (i.e. from 3.05GPa for HA to 4.25GPa for the composite film). Kim et al. [11] fabricated graphene–titania films with different graphene concentrations, from 0.1 to 1wt%, in order to improve energy conversion efficiency of a dye-sensitized solar cell. The 0.3%wt graphene showed minimum recombination rate with high photogenerated electron–hole pair formations. In both studies [11] and[50], AD films exhibited dense coating with uniform distributed components indicating the possibility of using graphene in AD method.

The literature review revealed a lack of studies on the application of AD for alumina-graphene composite coatings. Prior studies also investigated alumina as a ceramic powder to produce dense coatings using the AD method [48],[15][51][52]. Alumina/polymer composite coatings using AD have been studied extensively in the literature for example [53][54][55][7]. There is only one study by Akedo [21]in which he deposits alumina ceramic composites i.e. PZT-Al_2O_3 to explain the mechanism of crystallite size reduction during film coating. Given the gap in the current literature, this study contributes to the body-of-knowledge by offering AD method (as developed by [56]) for alumina graphene composite coatings.

2.4.   Microscale friction and scratch adhesion testing

The micro scratch test method is used to determine the mechanical failure mechanisms and adhesion strength of hard (Vickers Hardness HV = 5 GPa or higher), thin (≤30 μm), ceramic coatings on metal and ceramic substrates at room temperature [57].

The test procedure involves drawing a diamond stylus (Rockwell C)with a predetermined geometry (conical diamond indenter with a 120° included angle and a 200 μm spherical tip radius) across a coated test specimen's flat surface while applying a predetermined normal force (constant

or gradually increasing) over a given distance. Microscopically, the scratch track damage is evaluated as a function of the applied force. The typical stylus forces increase with certain degrees of progressive damage. The amount of force required to scratch a coating in a certain way is called the critical scratch load (s). The test method further defines the utilisation of tangential force and acoustic emission signals as a supplementary test data to distinguish among various coating damage levels. This method may be used for the purpose of analysing a wide variety of hard ceramic coating materials, such as carbides, nitrides, oxides, diamond, and diamond-like carbon, on ceramic as well as metal substrates [57].

Testing can be performed on coatings with thicknesses ranging from 0.1 to 30 micrometres. Test specimens generally always have a flat surface for the purpose of examination.

Because of the complex interaction between elastic and plastic indentation stresses, frictional forces, and residual internal stresses in the coating/substrate combination, stylus-induced mechanical damage to the coating and substrate is a function that grows with increasing normal force. Normal stylus forces are assessed with the different observable degrees of scratch track degradation. A critical scratch load is the usual force that causes a quantifiable and reproducible type/level of damage (L_C). One or more critical scratch loads (L_{CN}) may be calculated for a certain coating-substrate system, with each L_{CN} corresponding to a different level of coating damage. Figure 2-5 is a schematic representation of the adhesion scratch test apparatus and scratch procedure. This method has also been used on AD deposited coating to investigate the tribological properties of ceramic coatings. Lee et al. [52]compared the adhesion of alumina coating deposited by AD on different substrates. In this study, the acoustic emission signals of alumina coating were used to find the critical force on abraded or broken films. It revealed that emitted signals for alumina film deposited on Cu substrate were indicated above a normal load of 1.7 kgf while alumina film on sapphire substrate started to emit signals below a normal load of 0.5 kgf. Therefore, it was assumed alumina films deposited on sapphire substrates have a lower adhesion force than alumina films deposited on copper substrates. Figure 2-6 indicates the change in the acoustic signals of alumina film on Cu and sapphire substrates, respectively [52].
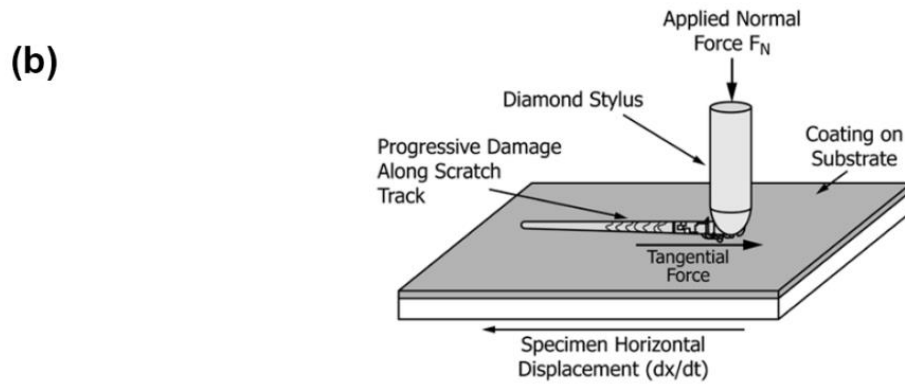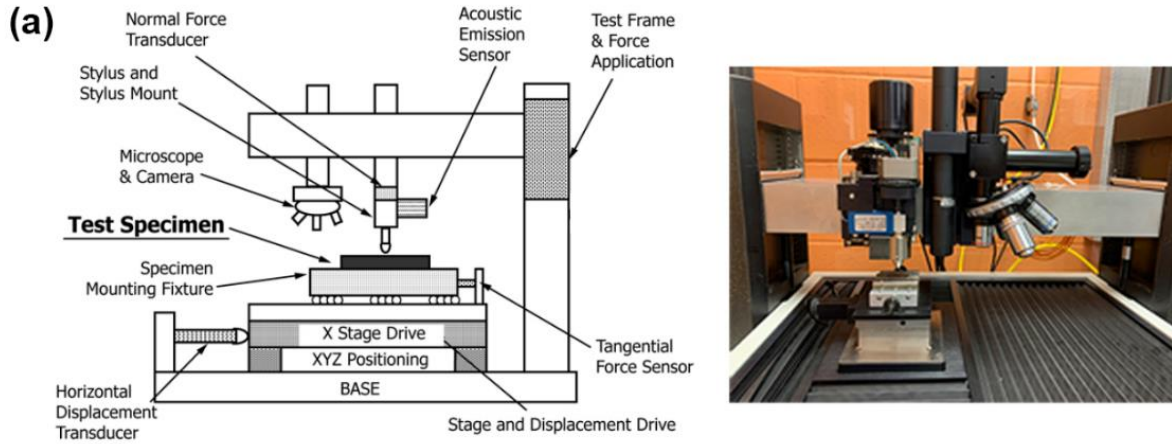
Figure 2-5: (a) Schematic of adhesion scratch test set up and (b) test method [57].
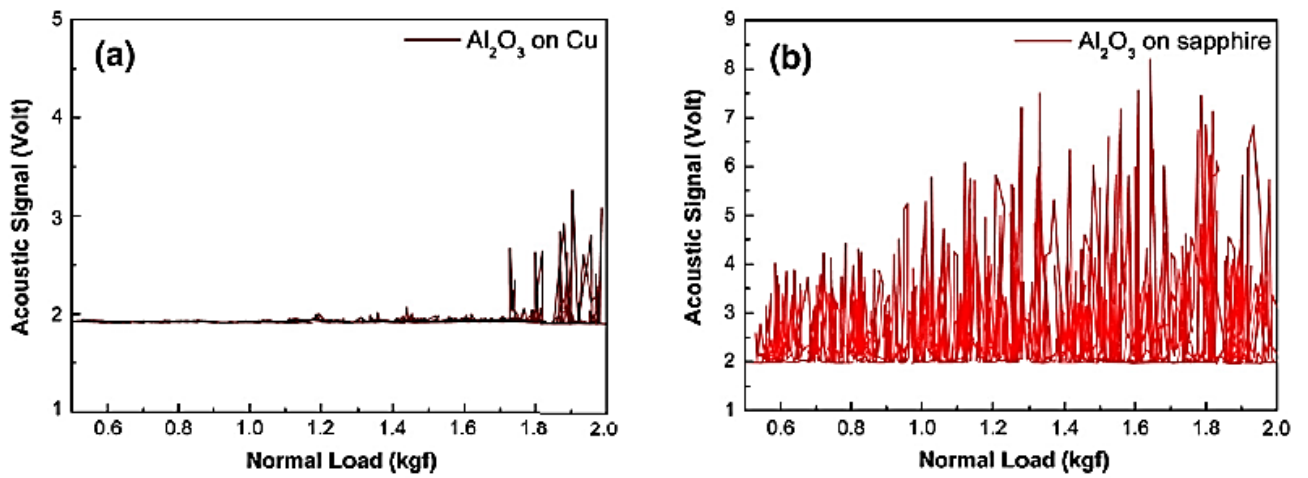
Figure 2-6: Acoustic emission changes of alumina coating on (a) copper and (b) sapphire substrates [52].

The scratch track analysis of Al2O3 films deposited on Cu and sapphire substrates indicated that Al_2O_3 films deposited on sapphire substrates had much lower adhesion than Al_2O_3 films deposited on Cu substrates. The findings of this investigation revealed a trace of a small scratch on aluminum coating deposited on copper at a 2 kgf load, while Al_2O_3 layer on sapphire substrates was fully worn away at 0.5 kgf force. Figure2-7 shows the SEM morphology results after scratch test. In Figure 2-7 it is evident that varying degrees of failure and fracture mechanisms occurred between alumina coated on cupper and on sapphire [52].
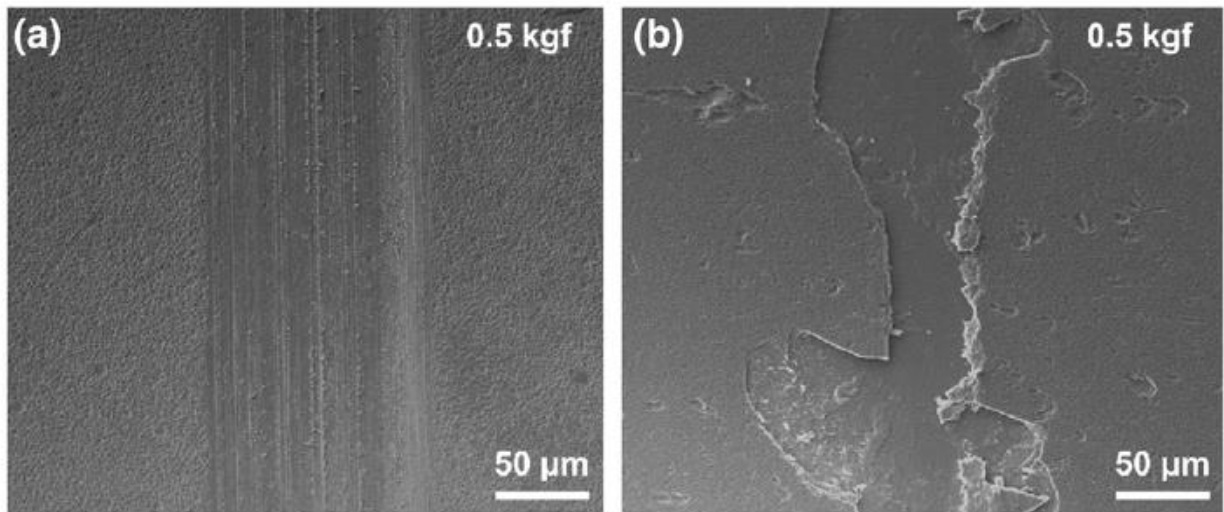
Figure 2-7: SEM images of (a) an alumina coating on a copper substrate that has been partially worn by 0.5 kgf loads and (b) an alumina coated on sapphire that has been totally worn by 0.5 kgf loads [52].

In this study, in order to assess the effect of adding GNP on tribological behavior of coating in comparison to pure alumina coating, the adhesion scratch test has been utilized. In the following chapter, the details of experiments and results of feedstock powder preparation will be discussed.

Chapter 3. Experimental Procedure

In this study, an in-house vacuum cold spray machine has been used. This machine was designed, built, and modified in the Mechanical, Industrial & Aerospace Engineering Department of Concordia University. To obtain the best operating conditions of the machine, different parameters have been tested and in order to improve the setup, some parts were modified/replaced to increase the quality and efficiency of coating. Spraying parameters and powder preparation are recognized as important factors in achieving an acceptable deposition and have been considered as the main two parameters in this study. In this study, to verify the spraying set up, alumina powder was tested and the best setup and test conditions were then applied to depositing a composite of alumina and graphene nanoplateles.

In terms of spraying features, the effect of stand-off distance, number of passes and substrate material were studied. The vacuum pressure of the deposition chamber was set at approximately 1 Torr and N_2 was eventually used as the carrier gas. The carrier gas flow rate has been kept constant at 5 l/min.

For the alumina powder preparation, the wet milling process was used to create more submicron cracks in the powder crystal structure. Since this work is performed with a composite of alumina and graphene nanoplatelets, the powders were mixed before introducing the powder into the aerosol chamber. This is an essential key for making the composite coating. Ball milling was chosen to reduce the particle size of the grapheme nanoplatelets and to disperse them with the alumina particles.

3.1. Substrate preparation

The substrate material of the samples used in this work was stainless steel (McMaster-Carr,USA).Flat steel substrates were prepared in sizes of 2.54 ×2.54× 0.3 cm. Prior to the coating process, the substrates were ultrasonically cleaned in acetone and dried with compressed air to

eliminate contaminant. The roughness was measured with a profilometer (Mitutoyo, Japan) in the center of the samples, in the same orientation of scanning of the nozzle. The surface roughness of substrates was measured as Ra ≈ 0.072 μm.Figure3-1 shows the substrates size and SEM topography of the steel substrate before spraying. Once the substrates were placed and fixed on the sample holder, the sample holder was moved to the front of the nozzle inside the deposition chamber, ready to be sprayed.
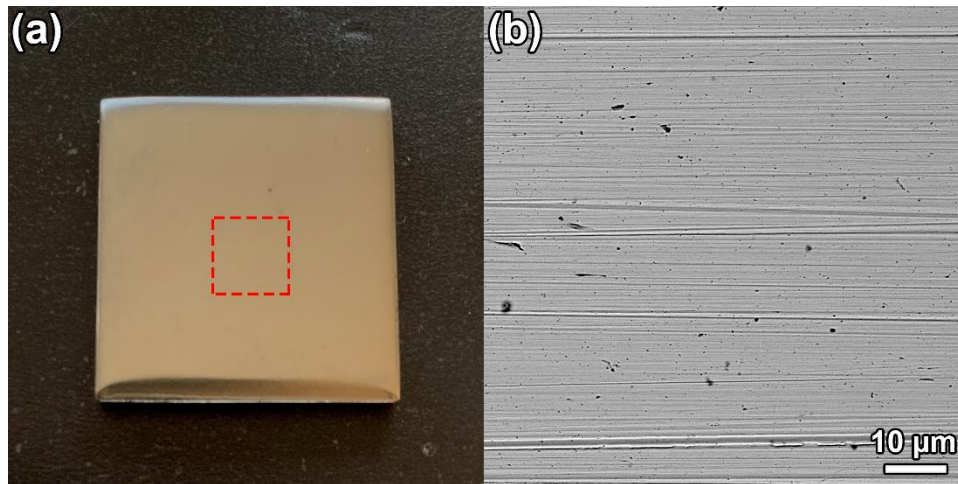
Figure 3-1 (a) Steel substrate and (b) the SEM images from the dashed area.

3.2. Powder preparation

Commercial alumina powders (Inframat® Advanced Material ™, Alfa Alumina- 99.9% , APS 0.4-0.5 micron) were used as the feedstock for the AD coating procedures. SEM micrographs of the as-received alumina are presented in Figure 3-2. In the SEM micrograph, alumina particles are shown to have a flat plate shape morphology. GrapheneBlack™ 3X (Nanoxplore Inc., Canada) which is a versatile and low-cost graphene powder with an average flake size of 38 μm with thicknesses ranging mainly from 6-10 layers was used as a reinforcement. TEM and SEM images of the as-received GNP are presented in Figure 3-3 showing the multilayer structure of graphene nanoplatelets.
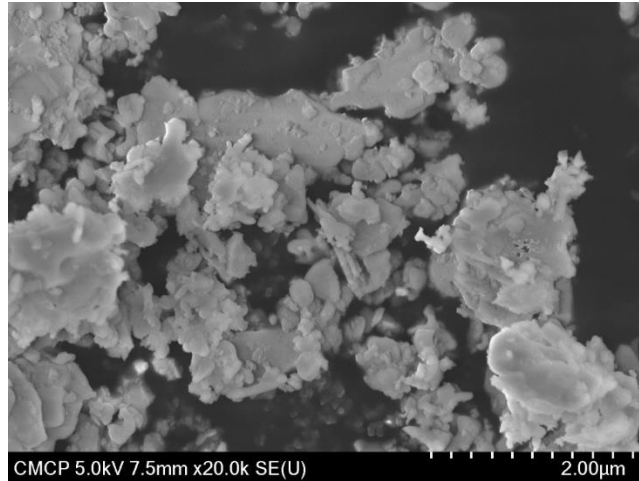
Figure 3-2: As received alumina powders with flat platelets morphology.
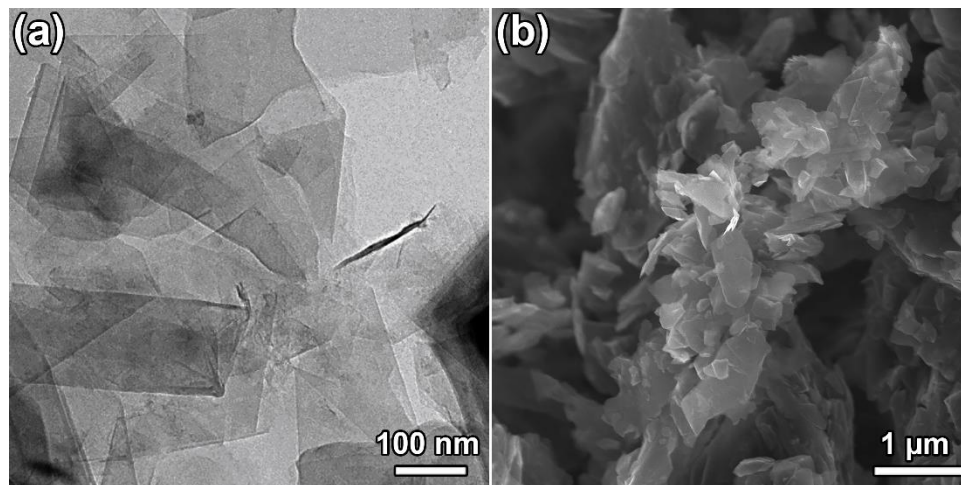
Figure 3-3: (a) TEM image of few-layer thick graphene flakes mainly from 6 - 10 layers

and (b) SEM image of GNP.

The negligible mass of GNP prevents it from generating sufficient momentum to deposit on the substrate. Therefore, alumina and GNP powder must be mixed together to create a composite powder before it can be introduced into the vacuum chamber.

High energy milling can be used to grind particles into a fine enough consistency for alumina deposition feedstock as this has been established as the preferred technique for producing fine alumina powder[58]. As a result, high energy planetary ball milling (QM- 3 SP04, Across International LLC) was used to grind the materials using zirconia jars and cyclohexane as the liquid for 4 hours. The liquid media was then evaporated by drying the milled materials within a fume hood for 24 hours. Analysis has also been done on the impact of milling duration on particle

size, microcracks and micro defects. Figure 3-5displays the x-ray diffraction (XRD) profiles of the as-received and milled alumina powders. It is clear from a comparison of two profiles that no peak shifting has taken place. It demonstrates that the alumina's phase was preserved following milling. Crystallite size reduction is achieved in high energy ball milling by high plastic deformation of powder. It could be shown by contrasting how each alumina peak's Full Width at Half Maximum (FWHM) broadens.
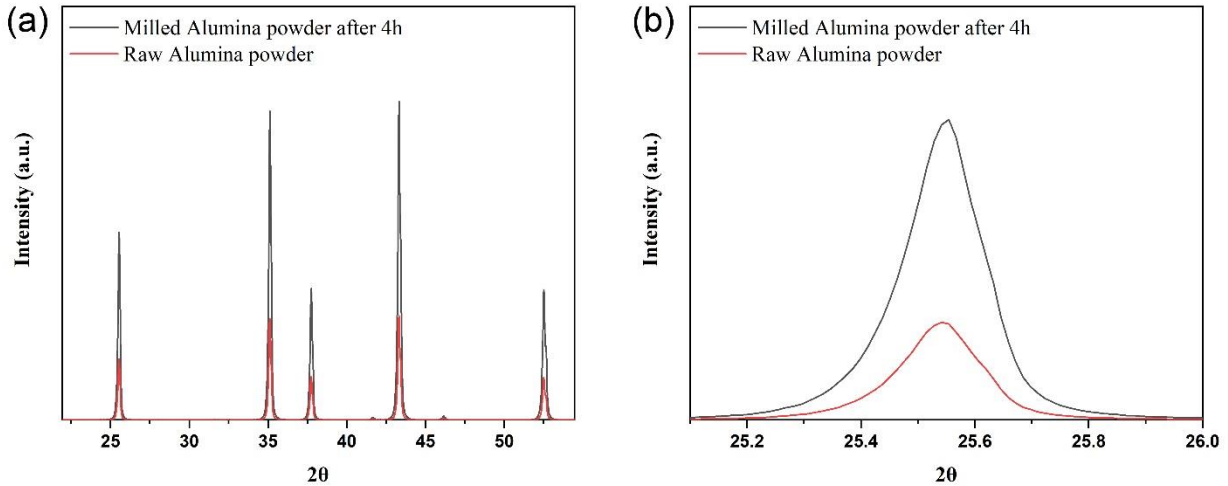
Figure 3-4: Comparison of X-Ray diffraction pattern of (a) raw and milled alumina powder, (b) comparison of broaden peak at 2θ=25.5.

Scherer equation has been used to determine nano crystallite size. The following Scherer equation is given in Equation 1, where D is crystallite size, K is the shape factor, which is often considered to be 0.89, λ is wavelength of the x-ray source, $K_{\alpha 1}$ = 0.15406 nm, β is full width at half maximum peak height and θ is peak angle. Also the dislocation density of powders have been calculated to compare the effect of high energy milling process. The explanations of these equations may be found, respectively, in Equations, which are listed below.

Scherrer equation

$$D = \frac{k\lambda}{\beta \cos \theta} \text{Equation 1}$$

Dislocation density

$$\delta = \frac{1}{D^2} \text{ Equation 2}$$

The differences in these characteristics between raw alumina powder and milled alumina powder are outlined in Table 3-1.

Table 3-1: Crystallite size and dislocation density of as-received and milled alumina powder.

Powder	Average crystallite size; D(nm)	Dislocation density ($1/nm^2$)
As received alumina	29	1.65
Milled alumina for 4 hours	26.5	2.25

While the density of dislocations has grown because of the addition of the high energy milling process, the average size of the crystallite has decreased small amount after milling.

The particle size distributions of all the powders were measured by a laser diffraction particle size analyzer (Malvern Instruments Ltd., England). According to the particle size distribution analysis of the as-received alumina and after it had been milled for four hours, the size of the alumina particles appears to have increased during milling. During milling and drying the powder agglomerated into larger clusters. As a result, the addition of a soft grinding procedure to refine and break up the particles was necessary in order to fragment soft agglomerated particles. The Dv(50) of milled powder was brought down from 1.84µm to 0.493µm for ground powder after being processed for an hour using polymer balls. It has been discovered that after grinding for one hour, the size of the particles is reduced to less than one micrometre, which mostly relates to the agglomerated parts (Figure 3-5). In order to check the effect of grinding time on the breaking of powder, 1 to 8 hours grinding have been tested. As Figure 3-6 shows, influence of grinding time is not changing after an hour.
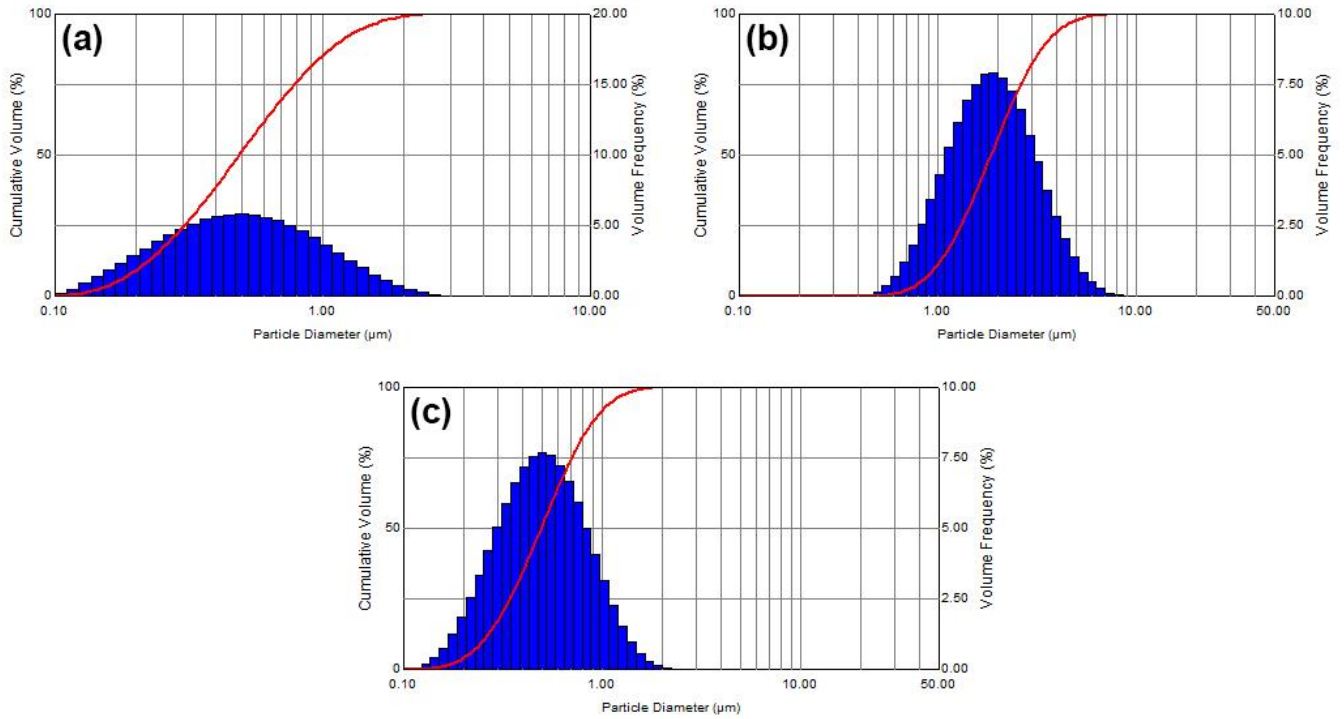
Figure 3-5: Particles size distribution of (a) raw alumina powder, (b) alumina milled powder after 4 hours (c) alumina milled powder after soft grinding for 1 hour.
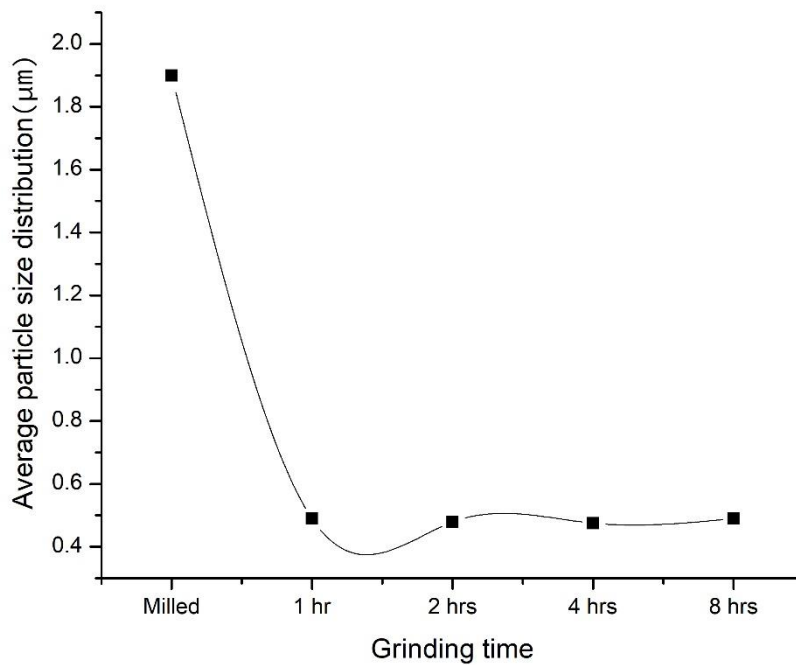
Figure 3-6 Effect of grinding time on average particles size distribution.

The remaining large agglomerated particles were separated by sieving with a mesh size of 75 μm, and the powder was then heated for 24 hours at 280 ℃ to create "aerosol" particles. The effect of grinding operation will be discussed in the next chapter.

To produceAl$_2$O$_3$-GNP coatings, 2 %wt of GNP with alumina had been milled for 4 hours in cyclohexane with powder to ball ratio of 1:2. Rotation speed has been adjusted to 250 rpm.

The particle size distribution of GNP and the Al$_2$O$_3$-GNPmixture are illustrated in Figure3-7 and 3-8 respectively. The size distribution characteristics of the feedstock powders revealed that the milled powders showed a noticeable size reduction in graphene nanoplatelets. The total large surface area of GNP can reduce the contact area between the Al$_2$O$_3$– Al$_2$O$_3$particles during the ball milling, which would then prevent the cold-welding of Al$_2$O$_3$ particles. This indicates that the graphene nanoplatelets can play a helpful role as grinding agent due to its small size and wrinkled structure, which can successfully prevent the agglomeration of mixture powders. Such prevention of the particle agglomeration facilitates the homogeneous distribution of the GNP within the Al$_2$O$_3$ matrix.
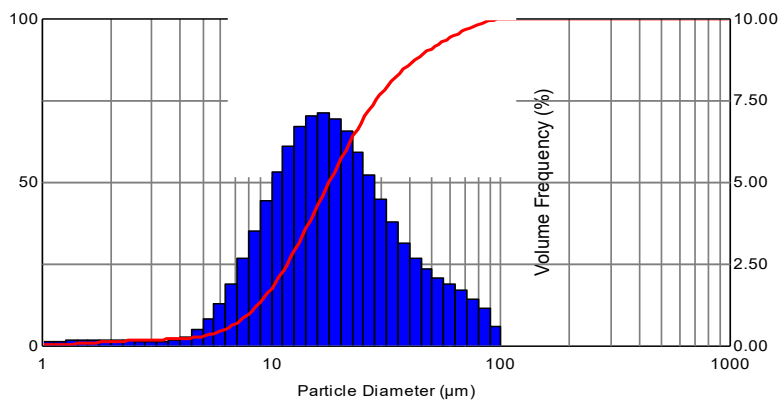
Figure 3-7: Particle size distribution of GNP.
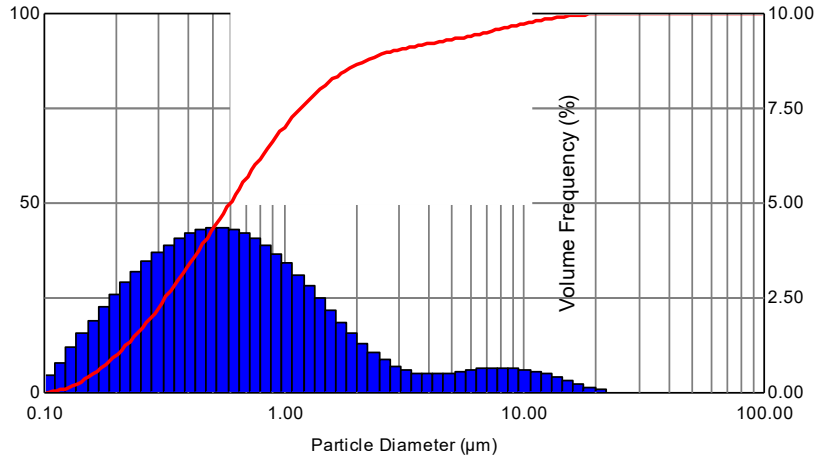
Figure 3-8: Particle size distribution of Alumina-GNP mixture after milling.

Table 3-2: Size distribution characteristics of Alumina as received, milled, grinded powder and Alumina-GNP used in the AD process

Powder	D_{10} (µm)	D_{50} (µm)	D_{90} (µm)
As received Alumina	0.207	0.487	1.15
Alumina milled	0.965	1.84	3.461
Alumina after soft grinding	0.251	0.493	0.948
Alumina-GNP after milling	0.201	0.592	2.782

The morphology of the milled powders was investigated with SEM and Raman Spectroscopy.

3.3. Design of experiments

In purpose to create successful coatings and estimate the effect of spray parameters on the quality of coats, stand-off distance and number of passes were chosen as variables.

Two stand-off distances (SOD) including 1.1and 11.3 mm have been tested for creating alumina coatings. These distances have been defined based on the geometry of the exit nozzle. The

geometry of the nozzle and calibration of the set up will be discussed in chapter 4.   In a series of experiments, the stand-off distance was selected to be 11.3 mm as this equals $5.5D_h$ where D_h is hydraulic diameter and was calculated as 2.05 mm. The vacuum pressure inside of the deposition chamber was adjusted to be ~1 torr (1.33×10^{-4} MPa). The spray conditions are presented in Table 3-3.

After milling, the wet powder was kept inside of the fume hood for 24 hrs to evaporate the cyclohexane. After evaporation, the agglomerated powder was broken up by soft grinding with polymer balls and then sieving was carried out through the 75 μm mesh. Then the treated powders were dried inside of the furnace for 24 hours at 280 ˚C. It worth to mention that in order to keep a constant agitation rate of particles for all experiments, vibration of the table in the aerosol generator was set in medium frequency.

As was mentioned earlier, the flow rate has a direct influence on particle velocity. High particle velocity increases the kinetic energy of the particles for impingement and consequently can generate erosion on the surface of the substrate. Hence, different flow rates from 2-20 l/min at a SOD of 11.3mm have been tested. On changing the flow rate from low to high, the kinetic energy of the particles increased and the lowly adhered coating became delaminated. Finally based on the geometry of nozzle, size of powder and pressure of deposition, the best results of alumina coating have been obtained at a flow rate of 5 l/min. This condition has been kept specifically for composite coating deposition.

Table 3-3: Deposition condition of alumina and alumina-GNP by AD

Powder	Alumina/ Alumina-GNP
Substrate	Stainless steel 304L
Carrier gas	N2
Carrier gas flow (l/min)	5
Scanning rate (mm/s)	0.9
Number of scanning	4 passes
Working pressure (torr)	0.9-1.2
Stand-off Distance	11.3
Deposition temperature	Room temperature
Frequency of vibration (Hz)	100

3.4. Coating characterization

To study the cross-sections of the coatings, the samples were cut using a precision cut-off machine (Secotom-15, Struers, Denmark), cold mounted in epoxy and then polished by standard metallographic procedures. The cut-off wheel used was 30A15 (aluminum oxide), selected according to the hardness of the material. The cutting program includes a rotational speed of 1500 rpm and a feed rate of the movable table at approximately 0.03 mm/s. Subsequently, the cleaned and dried sectioned samples were mounted in room-temperature curing resin. After curing, the mounted samples were polished in the Tegramin-25 polishing system to achieve a polished surface appropriate for metallurgical observations. The process started with wet grinding of the samples with 3 different grit silicon carbide grinding papers (320, 500 and 800). After grinding, additional polishing steps were performed to a final finish of 0.05 μm.

Once metallographic preparation was complete, the SEM microscope (Hitachi S-3400N, Japan) was used to take images from the surface and cross-section of the coatings to complete image analysis. The pictures recorded were taken with different magnifications. The image analyses of all the samples sprayed will be presented in Chapter 4. A 3-D Confocal Laser Scanning Microscope (CLSM) (LEXT-OLS4000, Olympus Corporation, Japan) was used for 3D topography imaging of the coatings and to measure the roughness of the coated samples. Raman spectrum was obtained using a Renishaw InVia Confocal Raman microscope with 514 nm argon ion laser radiation and a diffraction grating of 1800 1/mm. The scan was performed using three 30 second exposures.

To assess the adherence and friction coefficient of the coatings produced on stainless steel, a microscratch adhesion tester (CSM instruments, RST S/ N: 27-0497) was used. During the scratch test, acoustic emission, frictional force, and coefficient of friction were online recorded in a computer-based data capture system. Parameters of the scratch test are shown in Table 3-4. Further analysis and the results of this work are described in the following chapter.

Table 3-4: Scratch test parameters

Parameter	
Test type	Progressive
Begin load (N)	0.3
End load (N)	30
Loading rate (N/min)	149
AE sensitivity	9
Indenter progress speed (mm/min)	10
Scratch length (mm)	2
Indenter type	Rockwell
Indenter material	Diamond
Indenter tip radius (μm)	200

Chapter 4.   Results and Discussion

As mentioned previously, the objective of this work was to investigate the effects of graphene nanoplatelets on the alumina coating microstructure and its friction behavior. This chapter will present the results after calibrating the setup and refining the spraying conditions, including the results of the Raman spectroscopy, micro scratch testing of both alumina coating and alumina-GNPs composite coating as well as their SEM analysis.

4.1.   Calibration Setup

Before starting the experiments, it is important to calibrate the AD apparatus. The contributing factors in effective deposition are known as carrier gas species, gas flow rates, stand-off distance between the nozzle and substrate, and the scan speed.

The functioning of the AD spraying system was validated through testing the main parameters mentioned above. The process of calibration to achieve the desired coating is discussed in detail in the Appendix I. A brief summary of the calibration process is provided below and also illustrated in Figure 4-1. At first, the functioning of the nozzle and deposition chamber was improved by modifying the pipe geometries and their connections to the deposition chamber. When the low vacuum condition was stabilized, the formation of vortex flow inside the aerosol chamber was modified by changing the design of the aerosol chamber as discussed in Appendix I. Some tests were conducted but no uniform coatings were obtained. Therefore, modifications to staring powder was initiated by preparing the staring powder using high energy ball milling and soft grinding to prevent high brittle fragmentation of alumina particles in impingement. In terms of the carrier gas impact, when compressed air was replaced by nitrogen, the desired coatings were fabricated in 10 mm of SOD. In order to achieve a better understanding of the influence of SOD, the distance between the nozzle and substrate was studied in relation to the exit geometry of the

28

nozzle. This section focuses only on the effects of the geometry of the nozzle and the stand-off distance.
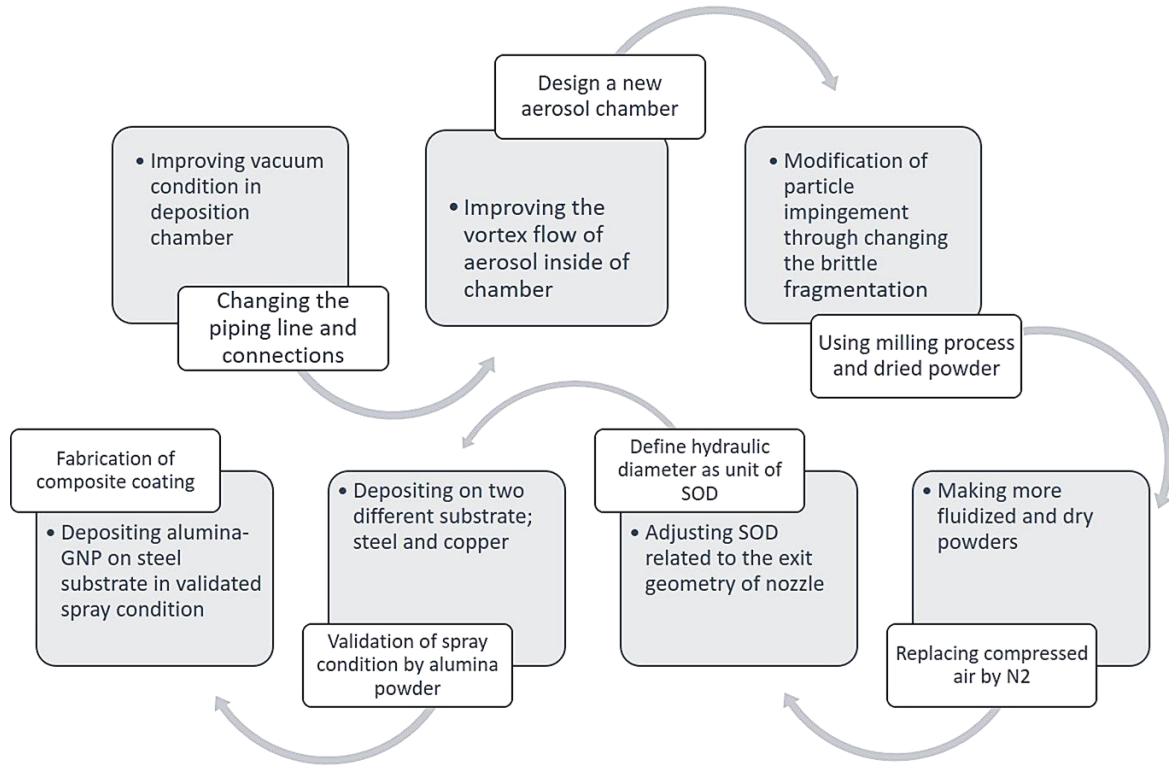
Figure 4-1: Sequential steps of calibration process for AD.

To describe the relation between the geometry of nozzle and the SOD, a series of experiments were performed. The geometry of the nozzle is depicted in Figure 4.2. Depending on the exit shape of a converging – diverging nozzle, the hydraulic diameter of nozzle was calculated by:

$$D_h = \frac{4S}{P}$$

where D_h is hydraulic diameter (mm), S is the sectional area of the exit nozzle (mm^2) and P is a wetted perimeter of the duct or pipe (mm). According to the geometry of our nozzle this diameter was calculated as 2.05 mm. This value was defined as a minimum factor distance between

nozzle and substrate. Since the limitation in the adjustment of the SOD in the current setup is around 12 mm, this value was chosen as a maximum allowable distance between the nozzle and substrate. The minimum and maximum distance in relation to the exit geometry can be defined as $0.5D_h$ and $5.5D_h$ respectively.

For the upcoming experiments, the short SOD distance to substrate was kept to $0.5D_h \approx$ 1mm, and for a long SOD was set to $5.5D_h \approx 11.3$ mm
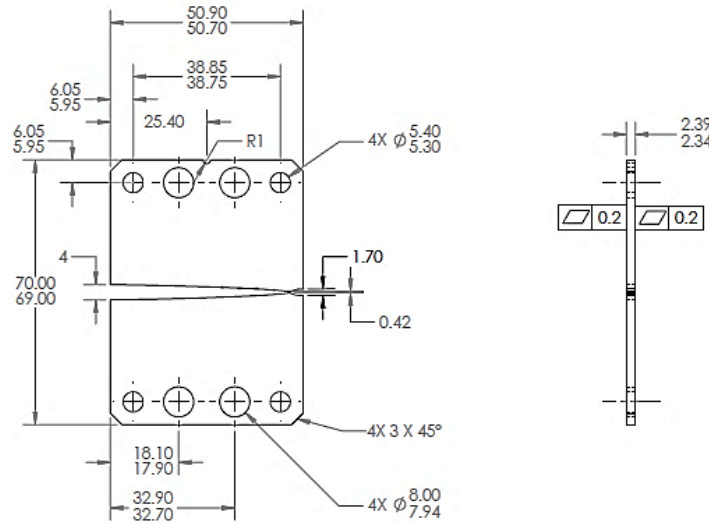
Figure 4-2: Geometry of converging- diverging nozzle (unites are in mm).

The spray conditions for all tests include 5 l/min N_2 gas flow rate, deposition pressure around 1 torr and 4 passes on a steel substrate. The obtained results showed that at the closest distance of $0.5D_h$, although some larger particles could bond to the substrate, the fine particles bounced from the surface of the substrate. In contrast, at a distance of $5.5D_h$, a uniform coating was obtained. The SEM images shown in Figure 4.3 and 4.4depict the top view and cross section of the coatings at $0.5D_h$ and $5.5D_h$SOD respectively.

A numerical simulation was used to describe the effect of stand-off distance on flow pattern and velocity of carrier gas. The simulation results indicated that shockwaves created by the nozzle's exit caused the carrier gas to expand. Gas velocity is decreased by increasing the stand-off distance. In both simulation cases from $0.5D_h$ to $5.5D_h$, when the gas approaches to the substrate, the axial velocity decreases since the static pressure on the substrate increases dramatically. This region which is called stagnation or deceleration region can significantly affect the particle velocity and

trajectory. At a SOD of 0.5D$_h$ in company with the effect of bow shock right before the substrate, the axial velocity of particles is less than for a SOD of 5.5Dh.
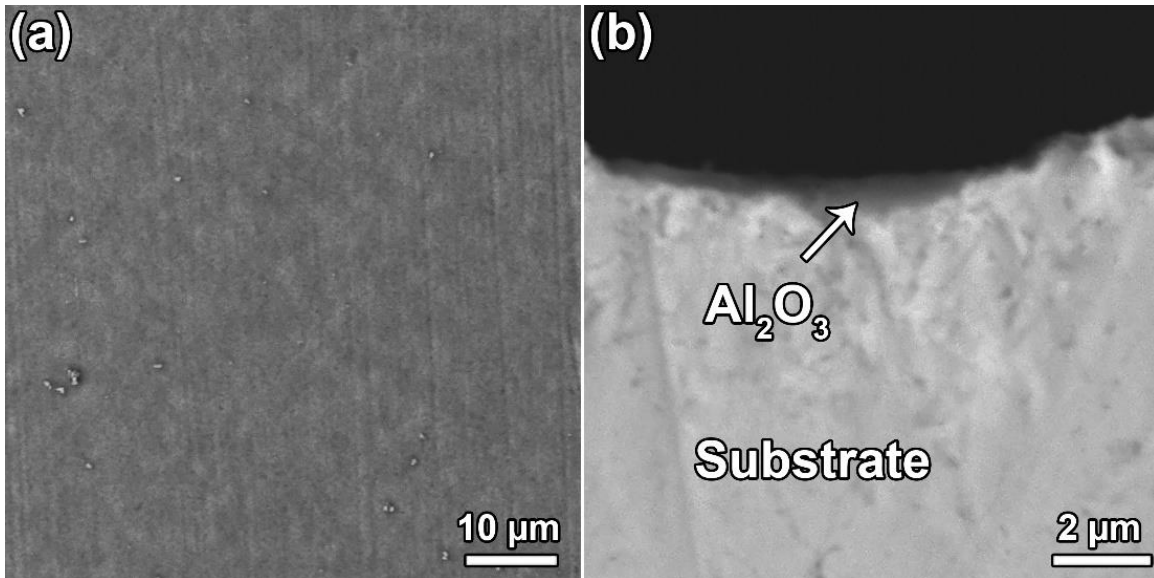
Figure 4-3: Alumina coating (a) top view of deposition particles and surface of substrate and (b) cross section of coating at 0.5Dh stand-off distance.
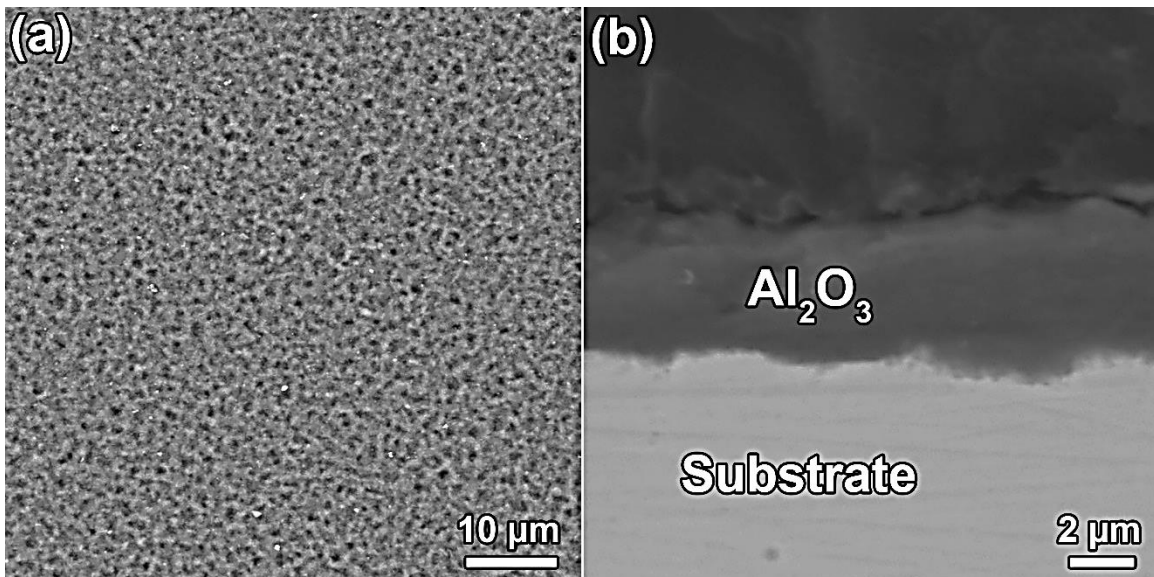
Figure 4-4: Alumina coating (a) top morphology and (b) cross section of deposited layers at SOD distance of 5.5Dh.

Therefore, in these two cases, it was concluded that for distances less than the hydraulic diameter of the nozzle, fine particles with low Stoke's numbers fluctuate and follow the gas streamlines without impacting the substrate, while at longer distances, particles achieve enough kinetic energy with appropriate axial velocity to impact surface substrate and form the coating. The numerical results of N_2 gas velocity and its flow streamline in two distances of $0.5D_h$ and $5.5D_h$ are illustrated in Figure 4.5.
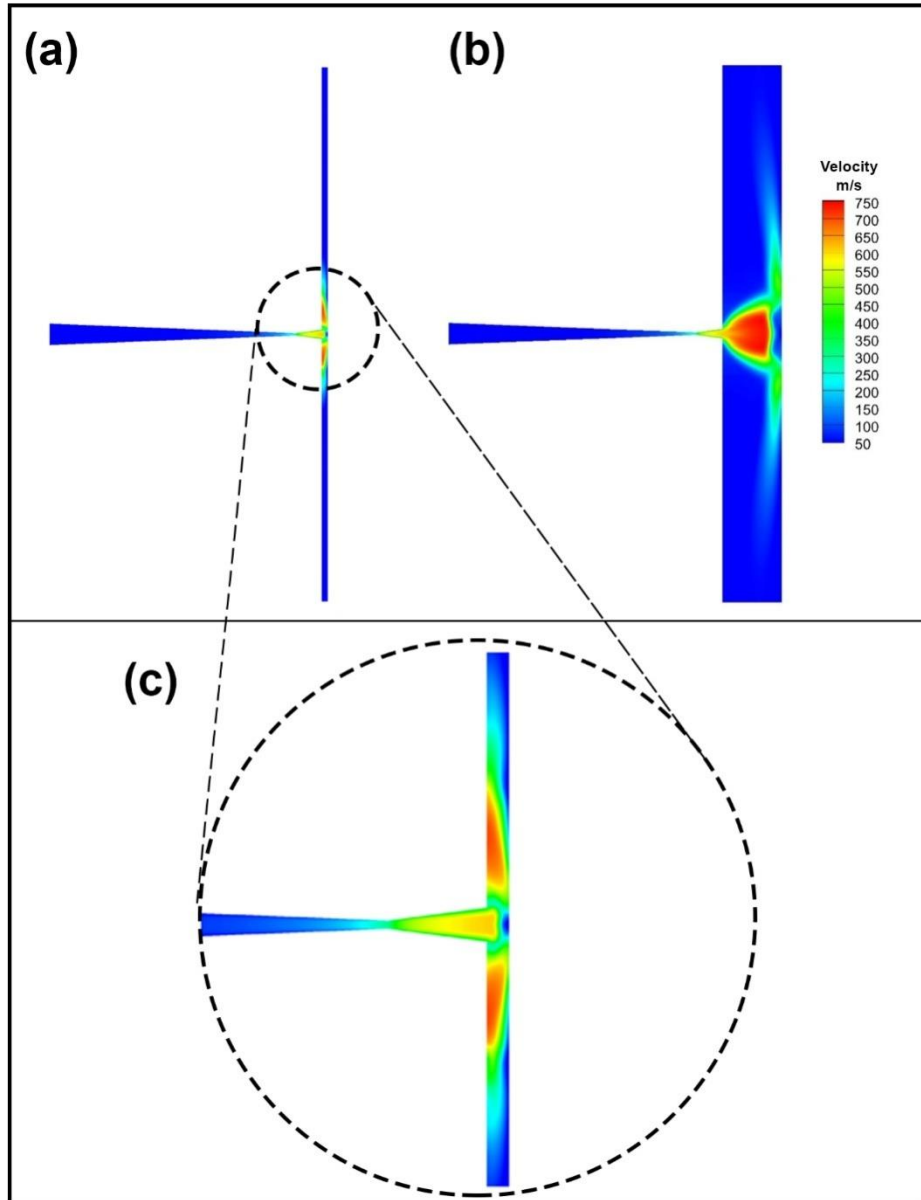
Figure 4-5: Velocity contours of N_2 gas flow in two stand-off distances; (a) $0.5D_h$, (b) $5.5D_h$ and (c) shows the magnified deceleration region of $0.5D_h$.

The axial centerline velocity of N_2 gas in both conditions is depicted in Figure 4.6. The velocity profile at the longer distance shows that the gas speed, right before the bow shock region, reaches to 750 m/s while the velocity at SOD of 0.5Dh is considerably lower and around 600 m/s.
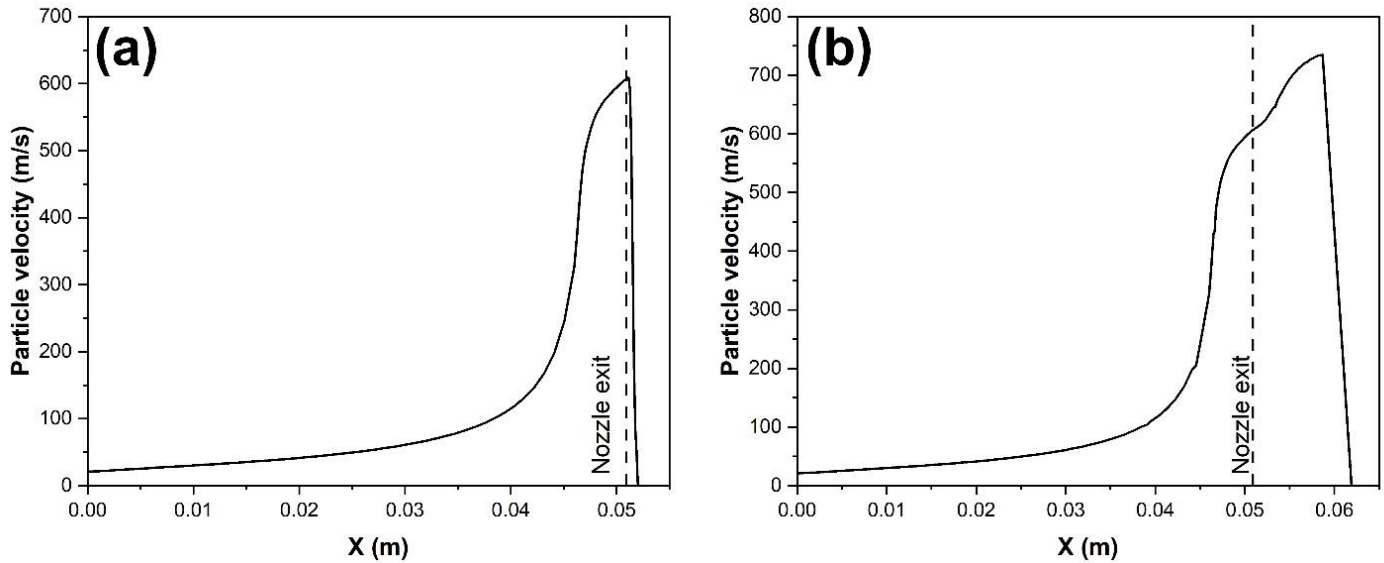
Figure 4-6:The axial velocity of carrier gas distance of (a) $0.5D_h$ and (b) $5.5D_h$.

The particle velocity at the landing location and in front of the substrate is illustrated in Figure 4.7. Figure 4.7 shows the distribution and velocity of particles before impinging on the substrate. It can be seen that the particle dispersion in the landing location for SOD of $0.5D_h$ is more than that of the $5.5D_h$SOD. The formation of strong bow shock and fully blocked flow at $0.5D_h$ results in the high level of particle dispersion. Particle velocity at $5.5D_h$SOD indicates that the strong shockwaves are suppressed and fine particles achieve the appropriate kinetic energy.

In conclusion, the experiment results and numerical outcome agree that the SOD of 5.5Dh (11.3 mm) is a decent operating distance for obtaining an acceptable coating. For distances between D_h and $5.5D_h$, the adhesion of particle-particle and particle-substrate were not sufficient to avoid delamination on coated area.

33
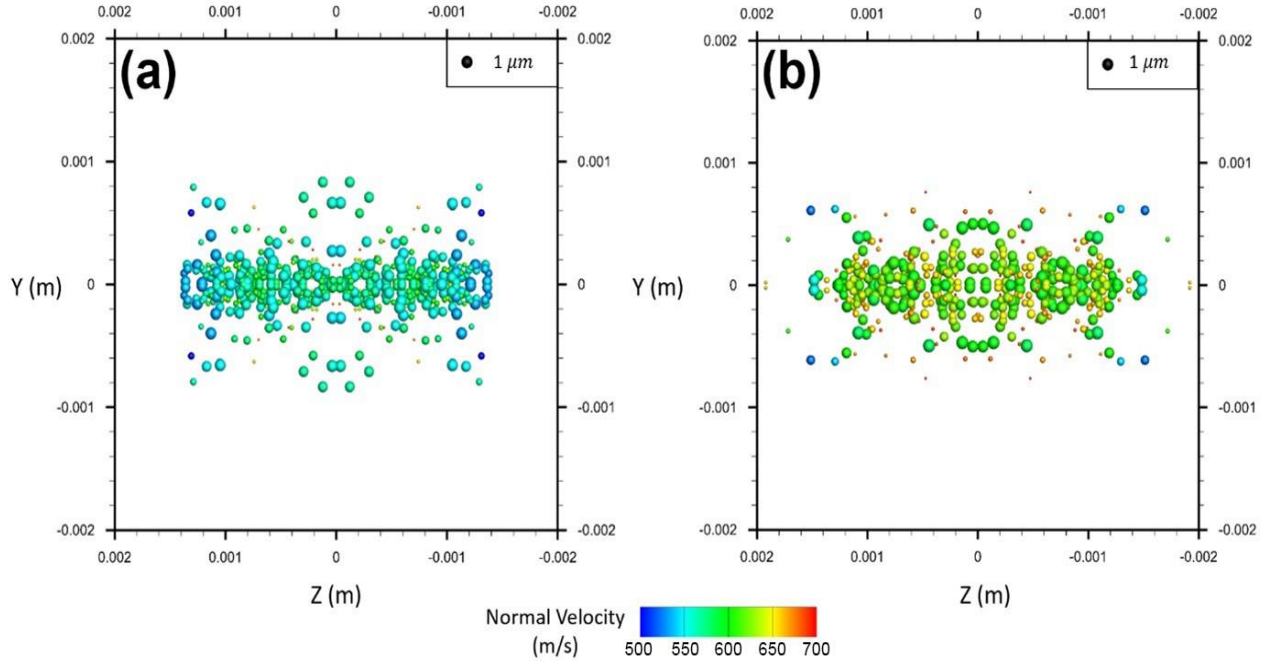
Figure 4-7: Landing location of particle and their velocities upon impact for two stand-off distances; (a) $0.5D_h$ and (b) $5.5D_h$.

4.2.   Raman spectroscopy

In order to further detect and confirm the presence of GNP in the prepared powder and coatings, as well as to determine the potential effect of high-speed deposition in AD on the structural properties of the GNP in the coating, Raman spectroscopy was performed in this study.

Three spectroscopic features represent the Raman spectrum of GNP. The G peak observed at 1580 cm^{-1} is attributed to the bond stretching of all pairs of sp2 atoms in chains and rings, the D peak at 1350 cm^{-1} characterizes the breathing modes of six-atom rings and the 2D peak shows the second order of the D band at ~2700 cm^{-1}. The G and D peaks in the Raman spectra are a direct indication of the existence of carbon materials[59]. From the Raman spectra presented in Figure 4-8, D and G peaks confirmed the retention of carbon material in the AD sprayed coating. The D peak intensity indicates the number of defects in the carbon material. Increased D peak intensity means increased defect density and edges[60].
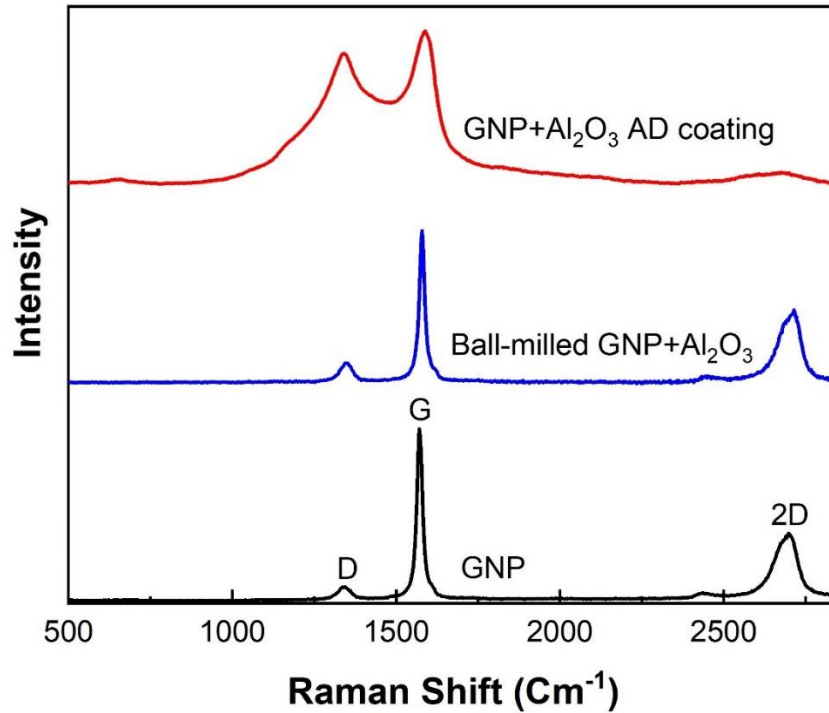
Figure 4-8: Mean Raman spectra of the unprocessed GNP, ball-milled GNP with Al_2O_3 before spraying, AD sprayed coatings containing GNP.

Figure 4-8 clearly demonstrates the differences in structural ordering in the GNP:when compared to unprocessed GNP, the D peak intensity rose dramatically in the AD coating, indicating that defects increased and the crystal size reduced following the AD process. However, the intensity of the D peak in high energy ball milling sample has not increased as much. It may be attributed to the lower applied load on particles in ball milling compared to the AD process. An increased ratio of D and G band intensities (I_D/ I_G) from ~ 0.1 to ~ 0.8 for AD was observed for the GNP. The obtained results correspond to the reduction in distance between defects which indicates the formation of additional defects in the GNP structure. It is important to note that an utterly disordered graphene layer may have an I_D/ I_G ratio of more than 3 [61].In addition, there is also significant change in the intensity, position or width of the 2D band following AD, which demonstrates that this procedure changed the number and orientation of graphitic layers in the GNP structure. Therefore, although there has been some increase in the disorder and decrease in crystal size, the intrinsic structural integrity of GNP can be well maintained in the coating process.

The comparison of the mean Raman spectra of the as-received GNP and ball-milled GNP showed there is some increase but this difference was not majorly significant. However, the slight increase in the I_D/I_G ratio of milled GNPcan be related to cold welding and fracturing actions of the ball milling process [62]. Totally, the structural damage of GNP can be reduced by controlling the rotating speed and an appropriate method[63][64].

The morphology of the fabricated alumina-GNP composite powder (2.0 Wt. % GNP) can be seen in the SEM image presented in Figure 4-9. As shown, the fabricated composite powders exhibited a layered flake-like structure. The morphology of the alumina powder observed the high-energy impact from the ball-powder-ball collisions compacts the platelet powders. Feedstock particles are shown to have a homogeneous distribution of GNP embedded in the alumina matrix.
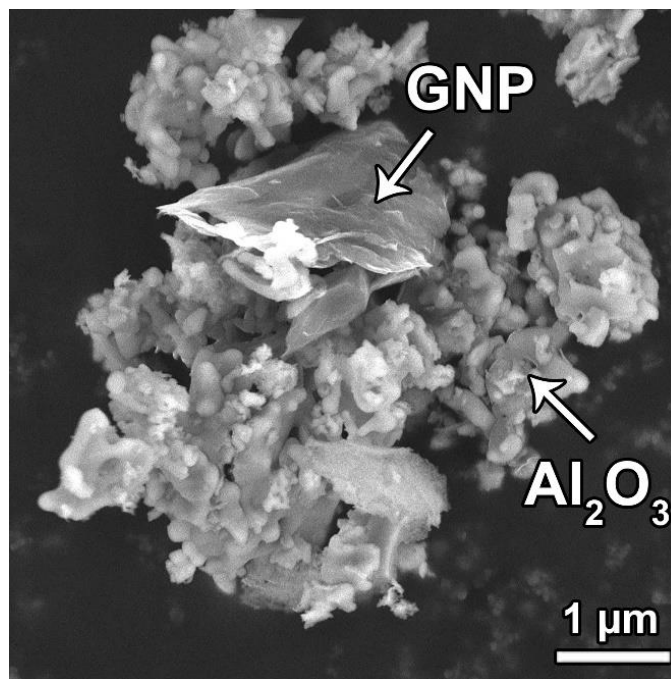
Figure 4-9: The SEM morphology of the ball-milled alumina-GNP.

4.3. Morphological studies

4.3.1. Alumina coatings by AD

As discussed before, powder preparation is an important factor for AD deposition. Hence, the effect of powder preparation including the high energy milling and additional soft grinding process on the deposition of alumina coating will be discussed. The cross sections of alumina coatings are shown in the SEM micrograph of Figure 4-10. Figure 4-10a illustrates the cross section of alumina powder subjected only to high energy ball milling for 4 hours. In figure 4-10b, deposition was implemented after an additional 1 hr of soft grinding (SG)of the milled powder. In Figure 4-10a, inside the deposited layer, a few microcracks are observed, possibly due to high film stress and then spread to the upper layers. In contrast, dense layers of coating were formed by utilising the soft ground powder, in Figure 4-10b. Additionally, in deposition layers with soft ground powder, the morphology of dense layers indicates entirely broken and hammered particles. Figure 4-11 shows surface morphology of alumina coating deposited from milled powder (4-11a) and milled+ SG powder (4-11b)
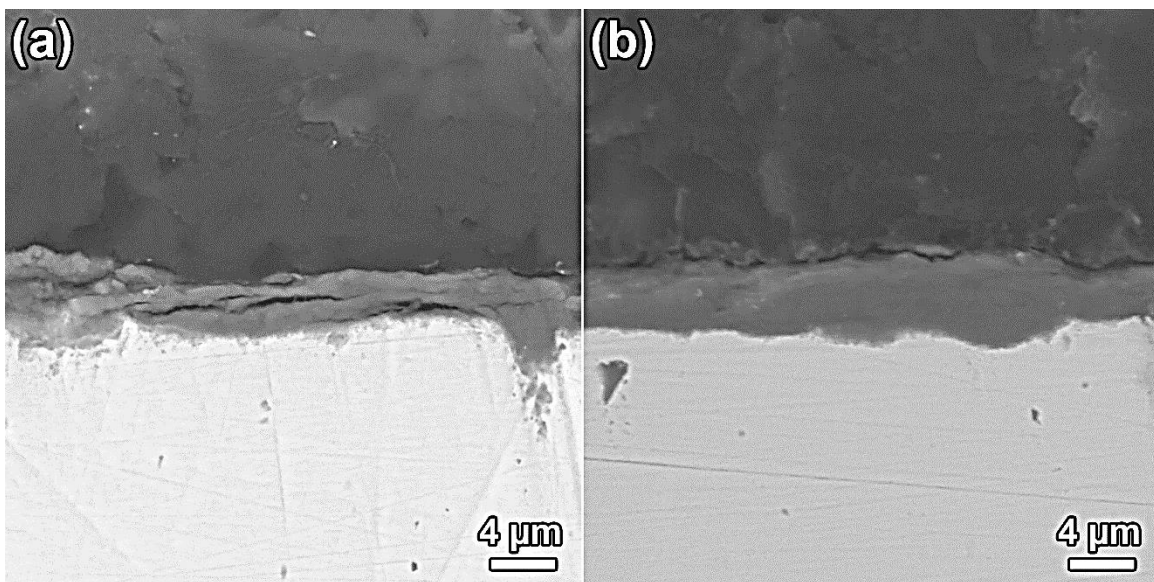
Figure 4-10: SEM micrographs of the alumina coating with (a) high energy milled powder

(b) milled+ soft ground powder for an hour.

In top view of coatings, different morphology between alumina coating with milled powder and milled+ SG powder is observed. More uniformity of coating in Figure 4-11b shows the SG process caused more breaking in agglomerated particles and prepared more small particle size for spraying.
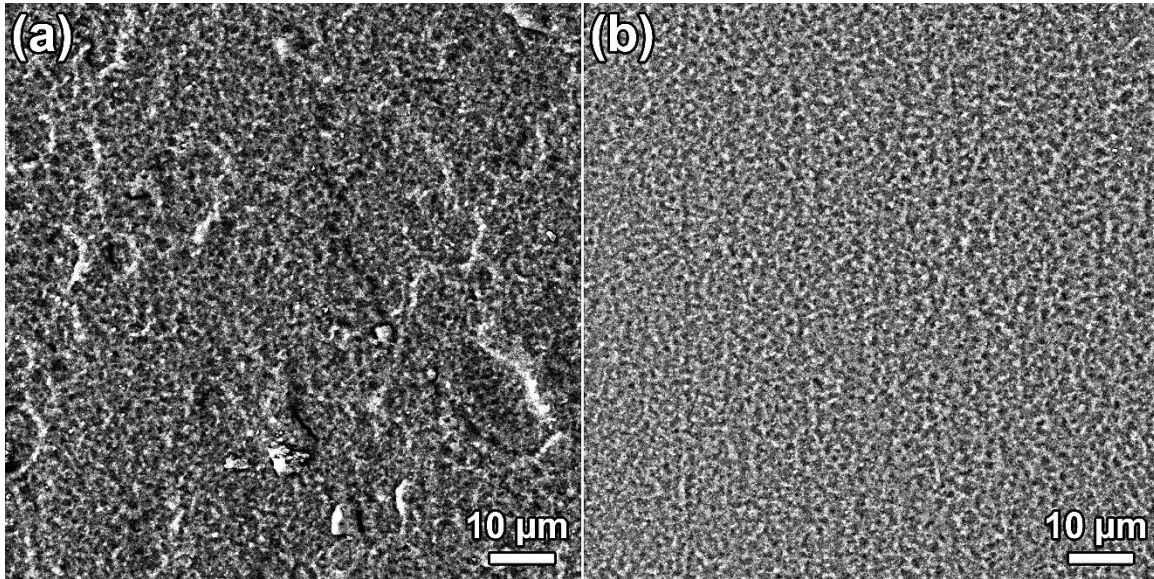
Figure 4-11: Top view of alumina coating with (a) high energy milled powder (b) milled +soft ground powder for an hour.

4.3.2. Alumina-GNP coatings by AD

Figure 4-12 shows a representative scanning electron microscopy (SEM) image of Al_2O_3-GNP 2wt% on a steel substrate. The corresponding energy dispersive X-ray spectroscopy (EDX) elemental mapping results are also illustrated in Figure 4-12. The findings of the elemental mapping show that the elements C, O, Al, and Fe exist, which suggests that graphene nanoplates are distributed in the composite coating. Throughout the whole coating, C atoms were distributed uniformly.

The SEM image of the cross section of Al_2O_3-GNP in Figure 4-13 shows composite coating of graphene nanoplatelets and alumina matrix, which makes a strong bond between GNP and alumina and creates a fully dense and crack-free coating.
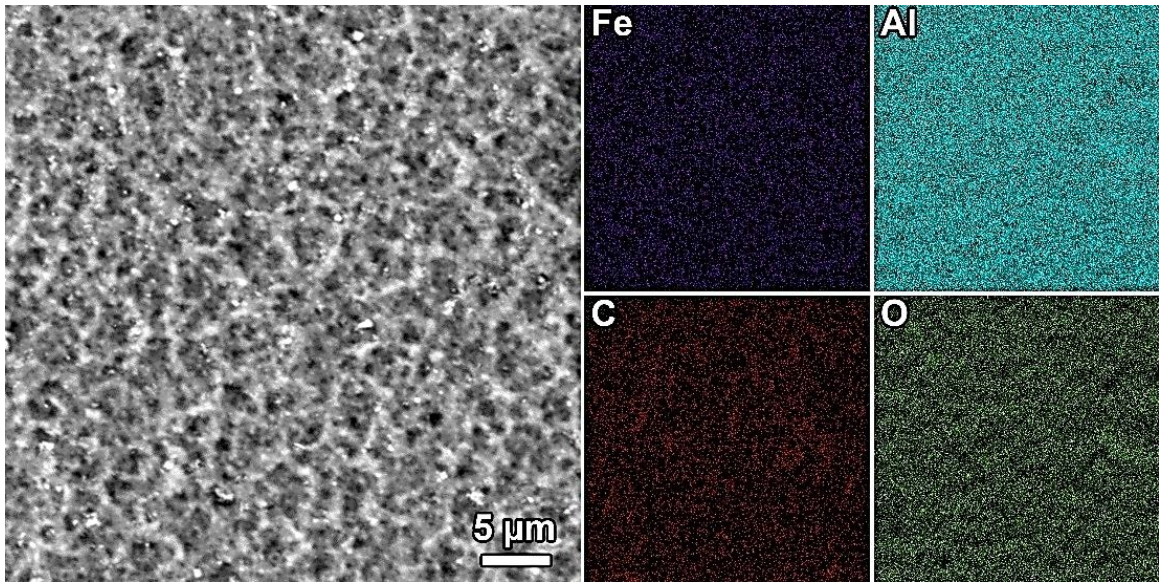
Figure 4-12: SEM image of the Al$_2$O$_3$-GNP and EDX mapping including of C, O, Al and Fe.
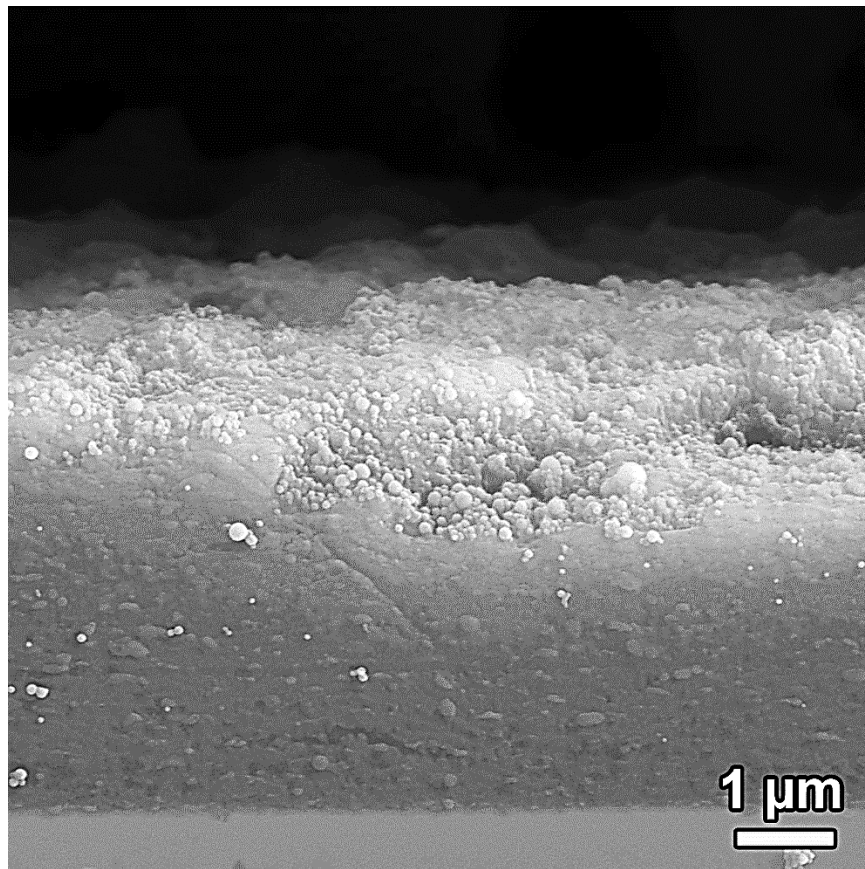
Figure 4-13: SEM image of cross section of the Al$_2$O$_3$ with 2 wt% of GNP.

4.4. Tribological analysis

Micro scratch tribological tests were carried out for Al_2O_3 and Al_2O_3-GNP coatings deposited on steel substrates in order to examine the impact of graphene nanoplatelets on the friction coefficient of Al_2O_3 + GNP coatings.

Scratching was achieved by raising the normal load from 0.3 N to 30 N, which was sufficient to break the deposited Al_2O_3 and Al_2O_3-GNP film which had a thickness of around 3-4μm. When the films were scratched, the resulting acoustic signals were captured and analysed.

Differences in acoustic signals between Al_2O_3 and Al_2O_3-GNP films on steel substrates are shown in Figure 4-14. Acoustic signals were produced by alumina films at loads considerably lower than the typical 6 N. This indicates that the yield point for Al_2O_3 films was at 5.7 N. The deposited Al_2O_3-GNP films, on the other hand, started generating acoustic signals around the normal load of 7.5N. Al_2O_3 films formed on substrates are considered to have weak adhesion forces in comparison to Al_2O_3-GNP.
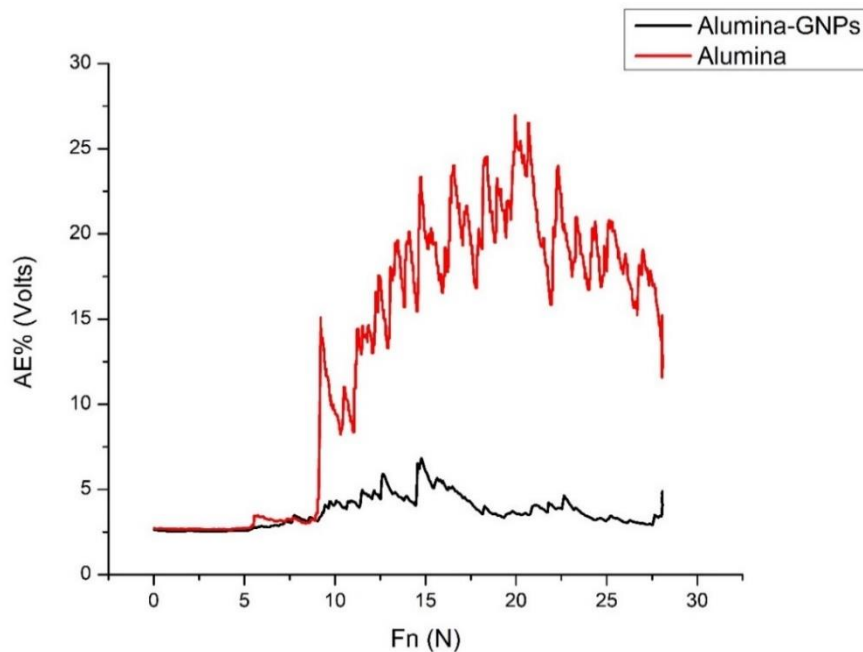
Figure 4-14: Acoustic emissions of Al_2O_3coating vs Al2O3-GNP under the normal load of 0.3-30N.

Results of the friction coefficient of the Al_2O_3 and Al_2O_3-GNP coatings along the scratch path are shown in Figure 4-15. In the scratch test carried on coatings, the coefficient of friction (COF) increased by increasing the applied load. Different trend can be seen between coefficient profile of Al_2O_3 and Al_2O_3-GNP coatings. In the Al_2O_3 coating, first, an initially rapid increase in friction coefficient, up to 0.12, was formed and sharply decreased to around 0.9. After that the friction of coefficient was increased by increasing the normal load. The result of quicker change in COF of Al_2O_3, indicates more destruction of the coating. It was previously believed that rough morphologies and broken films were responsible for these observed increases in friction coefficient [65]. In contrast, friction in the sliding path of the alumina-GNP increases with a gradual slope without the sharp rise and fall seen in the alumina. The COF curve of the Al_2O_3-GNP coating is consistently slightly slower than the Al_2O_3 coating.
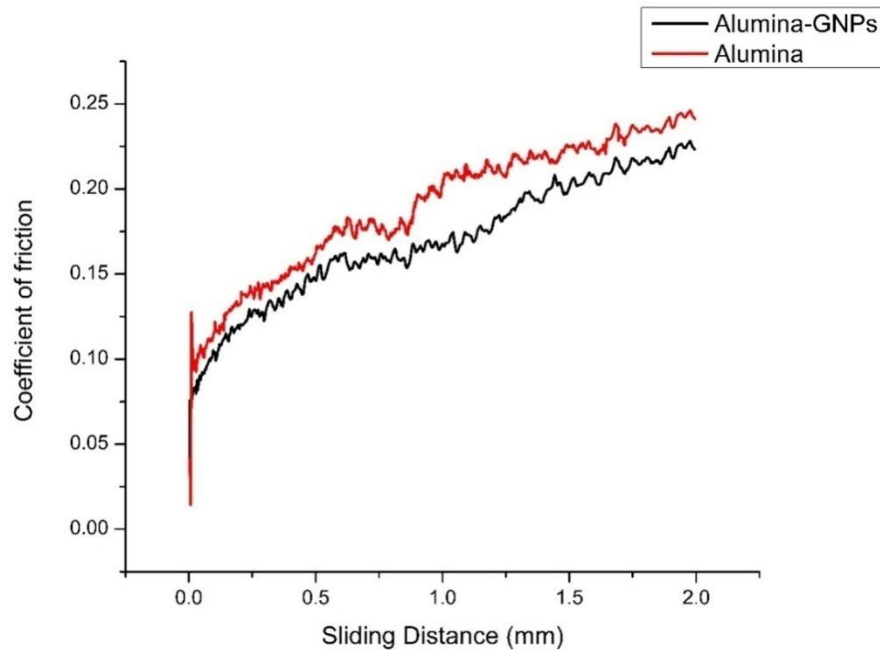
Figure 4-15:Friction coefficient changes of Al_2O_3coating and Al_2O_3-GNP during scratch test.

To investigate the effect of GNP on the friction coefficient, SEM images of sliding distance have been provided. Figure4-16and Figure 4-18show the SEM micrograph of the scratch track of $Al_2O_3$and Al_2O_3-GNP films deposited on steel substrates, respectively. In the alumina coating, arc tensile cracks were observed around 0.5 mm along the scratch axis from the start point (Figure 4-16b). This point could be linked to the first yield point of acoustic emission of alumina coating in

Figure 4-14which was associated with the stylus normal force equals to 5.7N. This point was defined as the first cluster of chevron cracks (L_{C1}).

Under the progressive load, different levels of damage in scratch track were created. At around 1 mm from the starting point, extension of tensile cracks formed conformal cracks which resulted in chipping failure. This is indicative of adhesive failure between the coating and the substrate. This point is inferred as L_{C2} (Figure 4-16c). At the end of the scratch track, bulk delamination of the coating at the border of scratch crack, which is characterized as recovery spallation, has occurred. In the middle of scratch's width, when the arcs were opened and away from the direction of scratching, buckling spallation and detaching of the film coating from the substrate were also observed (Figure 4-16d). It is also confirmed by EDX analysis from the region of delamination. Figure 4-17shows the EDX results from topology of scratch track on the alumina coating. Spectra 1 and 4 provide elemental analyses of the steel substrate, while spectra 2 and 3 display the coating composition as a high proportion of aluminium by atomic weight.

Figure 4-16: a) SEM image of scratch track on alumina coating, (b) surface view of arc tensile cracks indicated with white arrows, (c) chipping failure between coating and substrate, (d) bulk delamination and recovery spallation at the end of scratch track.

Spectrum	O	Al	Si	Cr	Fe	Ni
Spectrum 1	10.62	15.78	--	14.91	52.25	6.44
Spectrum 2	43.04	44.63	--	3.43	8.90	--
Spectrum 3	53.09	46.28	0.63	--	--	--
Spectrum 4	18.85	19.99	--	13.11	48.06	--
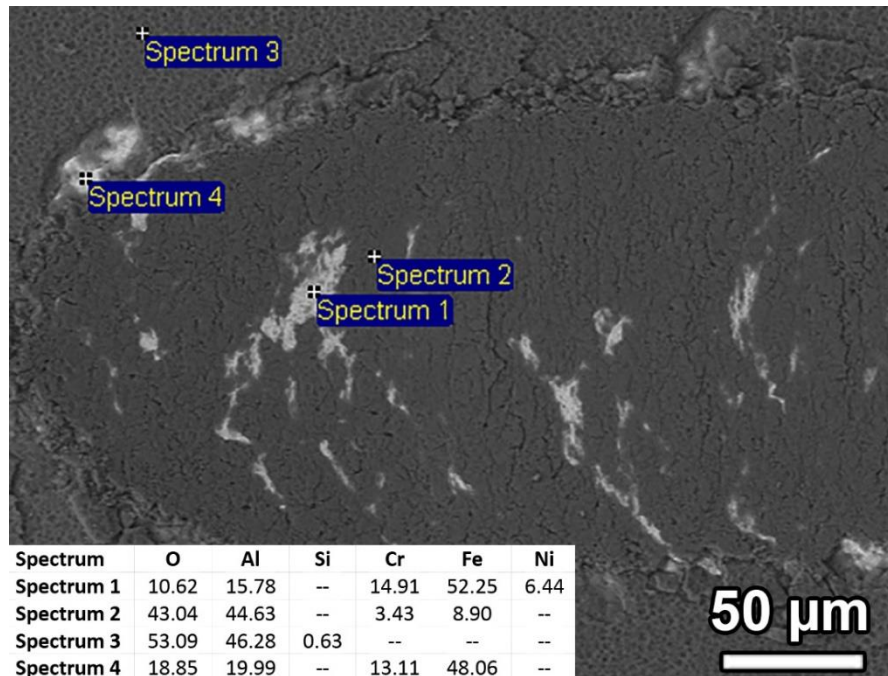
Figure 4-17: EDX analysis from worn region of alumina coating.

In the alumina-GNP coating scratch testing, a similar trend to the alumina coating was observed (Figure 4-18b and 4-18c) except at the range of the high normal force (Figure 4-18d). At around 0.5mm from the starting point of the sliding test, plastic deformation by the creation of the first arc tensile cracks was formed. Despite increasing the load, the deposited composite films indicted only a trace of a slight scratch along the sliding crack. It was clearly observed that at the end of scratched path, different degrees of failure and fracture modes existed. In the alumina-GNP coating, the coating next to the trace was still preserved despite the intense scratch force. No extensive delamination was observed in Figure 4-18d. Only forward chevron tensile cracks were observed in alumina-GNP coatings.

As an explanation, this may indicate a tribofilm of graphene, from the upper layer of the coating, was developed in the scratching process. It is proposed that under high normal stress of the friction test, graphene sheets from nanoplatelets are pulled under the shear and become welded with overlapping areas to form an ultrathin graphene tribofilm [66]. Due to the weak Van der Waals forces at the sliding contact surface, graphene shears easily.[67][68].
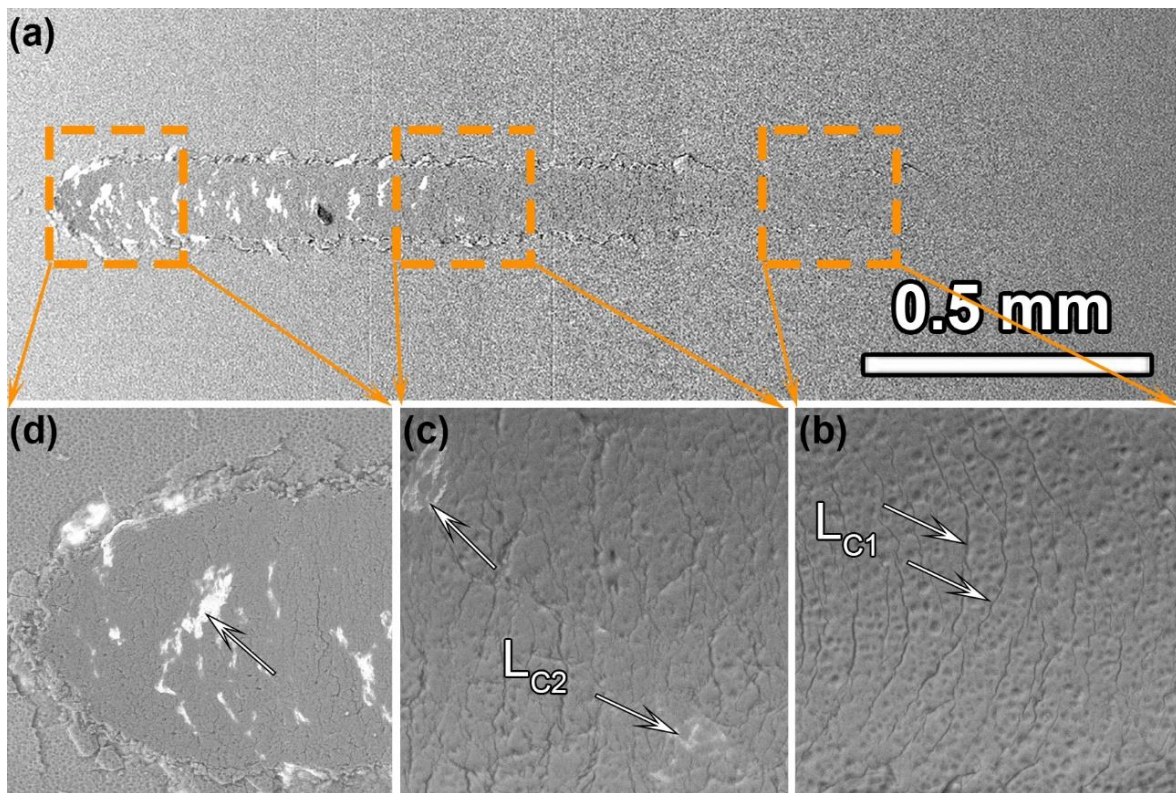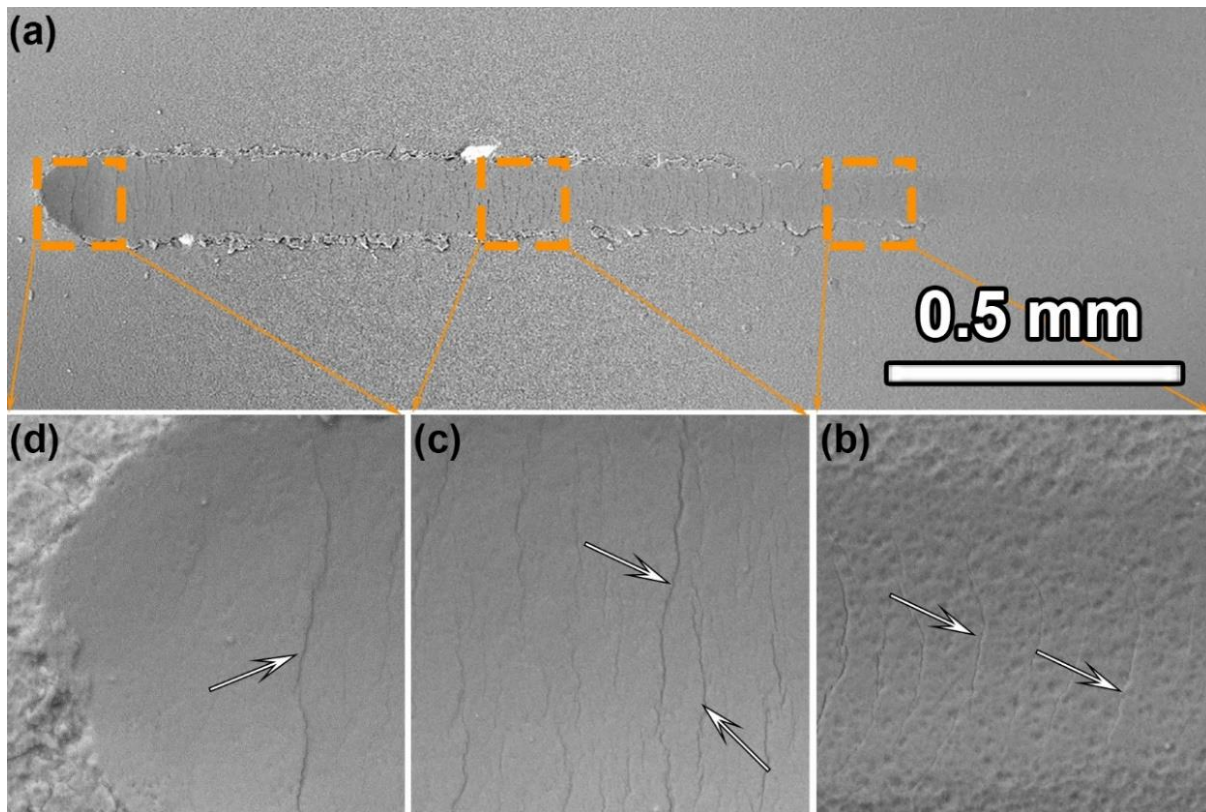
Figure 4-18: (a) SEM image of scratch track on alumina-GNP coating, (b) surface view of arc tensile cracks indicated with white arrows around 0.5mm from starting point, (c) conformal cracks around 1mm from starting point of crack, (d) End of sliding path without extensive delamination.

This phenomenon can be particularly effective when the GNPs are parallel to the plane of sliding surface, which in combination with the multilayer structure of GNPs, would allow the effective use of this slip mechanism proposed in the literature. [69]

The linear profiles taken from the cross of scratch path are shown in Figure 4-19. At a distance of 500 μm from the starting point, the alumina coating produces a depth of 1.5 μm, while the alumina-GNP coating provides a depth of around 0.5 μm. (Figure 4-19e). By raising the normal load, this difference is seen all along the scratch line, as shown by two more cross lines at a distance of 1250μm (Figure 4-19d) and 1900μm (Figure 4-19c).

Additionally, GNPs would be exfoliated and the layers would be pulled and dumped in their vicinity to produce lubricant films, therefore modifying the interface condition of the friction pair and favourably lowering friction at the contact surfaces. In the alumina coating, the local

micro cutting of the coating by a sliding stylus increases the abrasive particles, which increases the friction force and accelerates the wear of the coating.
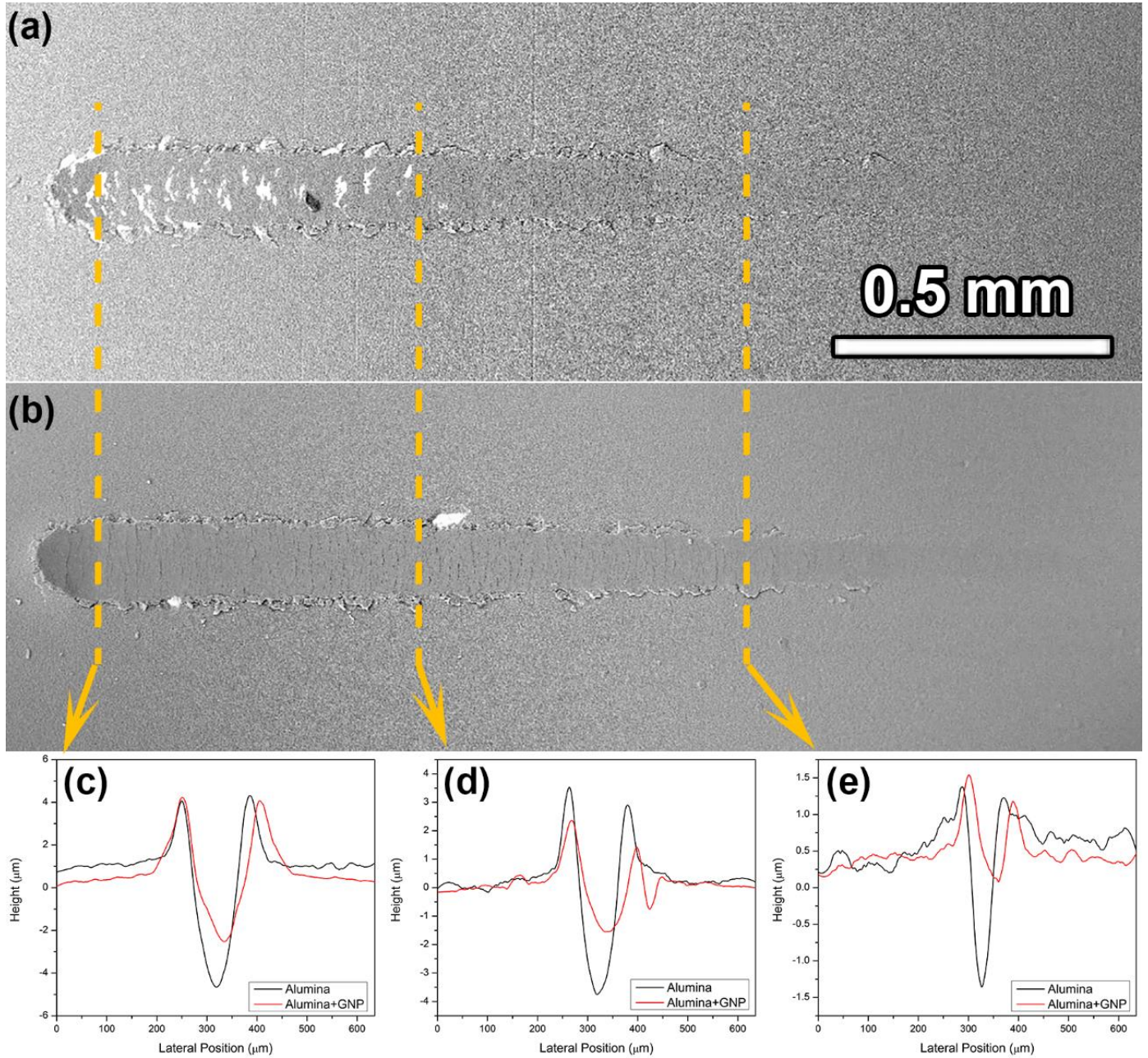
Figure 4-19: Scratch tracks on (a) the alumina and (b) alumina- GNP coatings with profiles of cross section of sliding track in distance of (c) 1900μm, (d) 1250μm and (c) 500μm from the starting point.

To determine the effect of the coating's surface texture, the roughness of both samples was assessed. Figure 4-20depicts the CLSM 3D surface topographies of the coated samples, with scanned surface areas of about 1800×1800 μm². The findings suggested that the alumina-coated samples had a higher surface roughness (Sa=517μm) than the alumina-GNPs coated samples (Sa=305μm). It could be concluded that the friction coefficient of the composite coatings was reduced by the cooperative effects of surface roughness and GNP additions.
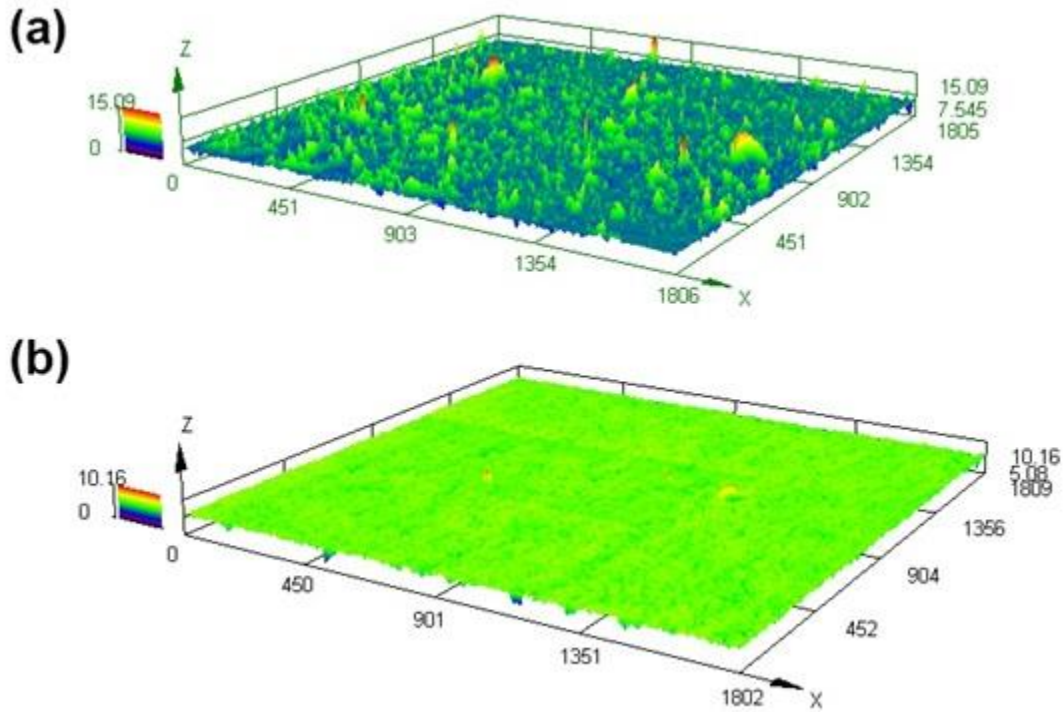
Figure 4-20:CLSM top surface topography of the coated samples, (a)alumina and (b)alumina + GNPs coating.

Chapter 5. Conclusions and Future Work

Alumina (Al$_2$O$_3$) is one of the most extensively used oxide materials for a wide range of applications due to its great mechanical strength and high hardness, chemical stability, strong thermal conductivity, and extremely low electrical conductivity. Not only it has been used in electric and electronic devices, reinforcing components, catalytic supports, medical implants, and thermal and wear-resistant components, but also it has been implemented in the form of coatings manufactured by different techniques such as thermal spraying, chemical vapour deposition, sputtering, sol-gel deposition. The most prevalent applications for alumina coating are as follows: protection against electrochemical and high-temperature corrosion, as well as reduction of wear.

The alumina coating's chemical stability and hardness were used to evaluate the wear reduction performance, despite the fact that achieved coefficient friction of pure alumina coatings are relatively high. Several efforts have been undertaken to minimize the COF as it is an essential parameter to increase the coatings' durability and wear resistance. Coating additives provide the primary potential for improvement. Recently, graphite and graphene nanoplatelets (GPN) have been used to improve the mechanical and electrical characteristics of ceramic composites. When graphene nanoplateletsare equitably spread in the matrix of an alumina composite, the resulting material shows great promise as a reinforcing material and reduction of coefficient friction of composite coatings. Thermal spraying techniques provide alumina+GNP coatings with insufficient control over GNP dispersion and alumina matrix phase transfer. Determining the tribological characteristics of an alumina-GNP coating was therefore motivated by the aforementioned concerns and the prospect of developing a dense and compact composite coating using the AD method.

Therefore, this experimental research was performed to yield an alumina-GNP coating and develop the friction behaviour of the coating. To investigate the effects of the addition of graphene nanoplatelets on the microstructure and friction behavior, alumina and an alumina composite coating with 2 wt% of GNPs were fabricated by aerosol deposition on steel substrates. The spraying developments with the purpose of maximizing the adhesion of coating have been carried

out to enhance the uniformity and density of coatings. Before depositing the powder, several processes have been conducted to prepare the feedstock of powder. Ball milling for 4 hours in wet media and soft grinding of the dried powders, were deemed as the best process to prepare the appropriate particle size powder for spraying.

Different spray parameters were tested and it became apparent that the stand-off distance as related to the geometry of the nozzle was very important if a well-adhered coating was to be obtained.

Once these parameters were established, GNPs were added to the alumina to determine its impact on the microstructure and properties of the final coating. To reduce the particle size and distribute the added GNPs between the alumina particles, milling processes with drying treatments have been carried out. With controlling the powder treatment and spray parameters, GNP embedded in the alumina matrix was produced. Raman analysis further demonstrates the presence of GNP in the coating while the defects in its structure increased after AD processing. Further characterization to assess friction coefficient and wear behavior showed alumina-GNP coating improves the wear behavior of the coating.

With these observations, it can be concluded that, for this work, the GNP could be preserved in the coating process and the aerosol deposition method is a good candidate to deposit thin alumina-GNP coatings because of the dense coating fabricated at low temperatures and well distributed GNPs in the alumina matrix. The micro scratch test results showed a reduction in the coefficient of friction due to the addition of GNPs in applied loading between 0.3 and 30 N. In the alumina coating, a high degree of delamination occurred, whilst in alumina-GNP coatings, plastic flow of the coating created conformal arcs. Regarding the friction of coefficient, adding the GNPs lowered the friction when compared to the alumina coating.

- For future work, comparing the effect of adding more GNP to the alumina coating, to further improve the wear behavior of composite coatings would be interesting. Furthermore, another experimental work would be using carbon nanotubes (CNT) instead of GNP as additive.
- Additionally, the investigation of other mechanical properties like wear resistance and electrical properties of the coating can be considered valuable for industrial applications.

- An forthcoming research might also look at the influence of a longer SOD than $5.5D_h$ on the deposition of ceramic or composite coatings, as well as the distances between $0.5D_h$ and $5.5D_h$.

- Lastly, spraying the alumina+GNP coating on different types of substrate material, depending on their applications, can be explored.

Appendix

Appendix I: Calibration Setup

Prior to commencing the experiments, it is important to calibrate the AD apparatus. Key factors in effective deposition are known to include carrier gas species, gas flow rates, stand-off distance between the nozzle and substrate, and scan speed. Based on the literature, the deposition chamber pressure is typically maintained between 0.2 and 20 mbar (0.15 and 15 torr), and the pressure in the aerosol chamber has been reported from 60 to 1066 mbar. In addition, a range between 0.5mm and 50 mm has been used for the distance between the nozzle's exit and substrate surface (stand-off distance, SOD). Air, N_2, O_2, Ar and He have been the most frequently employed gases in AD. Gas flow rates used have been between 1 and 30 l/min and speed of scanning or sweep speed has been from 0.05 to 10 mm/s. Moreover, the shape and size of the nozzle must also be taken into account since they have an impact on the aerosol jet's particle velocity.

Therefore, the effects of main spraying parameters were examined through a series of experiments to obtain the best values for deposition. To validate the current AD machine, the performance of the vacuum pump, the aerosol chamber and the nozzle were tested. The commonly used alumina powder was selected for the calibration process. Two different metallic substrates were also used: copper as a soft metal and stainless steel as a hard substrate.

The pressure in the vacuum chamber was initially between 6 and 7 torr. (8 to 9.3 mbar). By modifying the piping and connections between the booster pump and the deposition chamber, the back pressure in the deposition chamber was improved dramatically to around 1 torr. The fluidized bed aerosol generator was used to deagglomerate particles in order to establish aerosolization of the micro-particles. The fluidized bed with a latex diaphragm allows the particles to be picked up by the gas flow that is coming from the mass flow controller. In this aerosol generator, compressed gas was fed into the fluidized bed from four injection nozzles. Several

experiments were conducted with this setup, but nonuniform coatings were obtained. Figure 6-1 shows the alumina particles deposited on the substrate in the initial experiments.
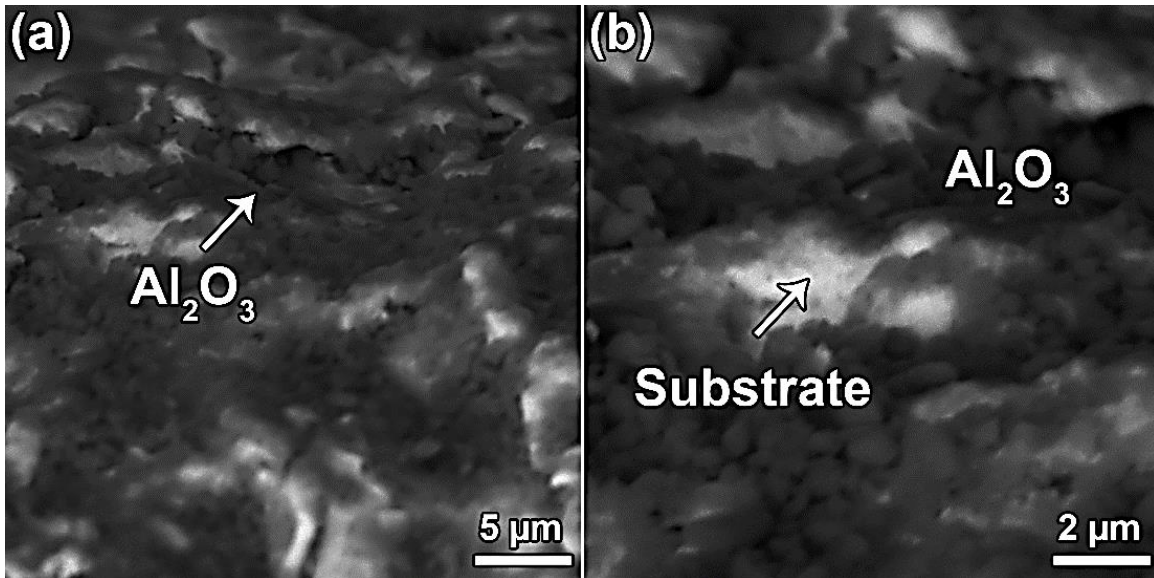

Figure 0-1: SEM Images of adhered particles on steel substrate with (a) 2.5k and (b) 5k magnifications.

Various factors, including stand-off distance, were investigated in conjunction with compressed air flow, but no acceptable coatings were obtained due to the low efficiency of the generated aerosol. Because low gas flow rates produce a low vortex flow of aerosol, the maximum flow rate that could be adjusted in the flowmeter, around 15 l/min, was used in this aerosol generator to fluidize the alumina particles. This high flow rate in the low pressure of deposition chamber (around 1 torr) caused high particle velocity and kinetic energy which affected the deposition behavior of particles. High gas flow rates agitate the big particles, and the high speed of the big particles creates high kinetic energy in their impingement on the substrate. Although this range of speeds produces a significant degree of particle fragmentation, it prevents the formation of subsequent layers (Figure 6-2). Fragmented powders in high fractions usually makes abrasive blasting on the surface, specially in the center of the scanning line, instead of making anchor layers. In areas far from the center of scanning line, the tangential speed assists to make some coating such as individual islands. These separated islands of coating might be the result of the surface roughness of the substrate and the speed of particles. Even though the quality of the

coating improved when the stand-off distance was raised from 5 to 10 mm, some delamination was still seen. (Figure 6-3).
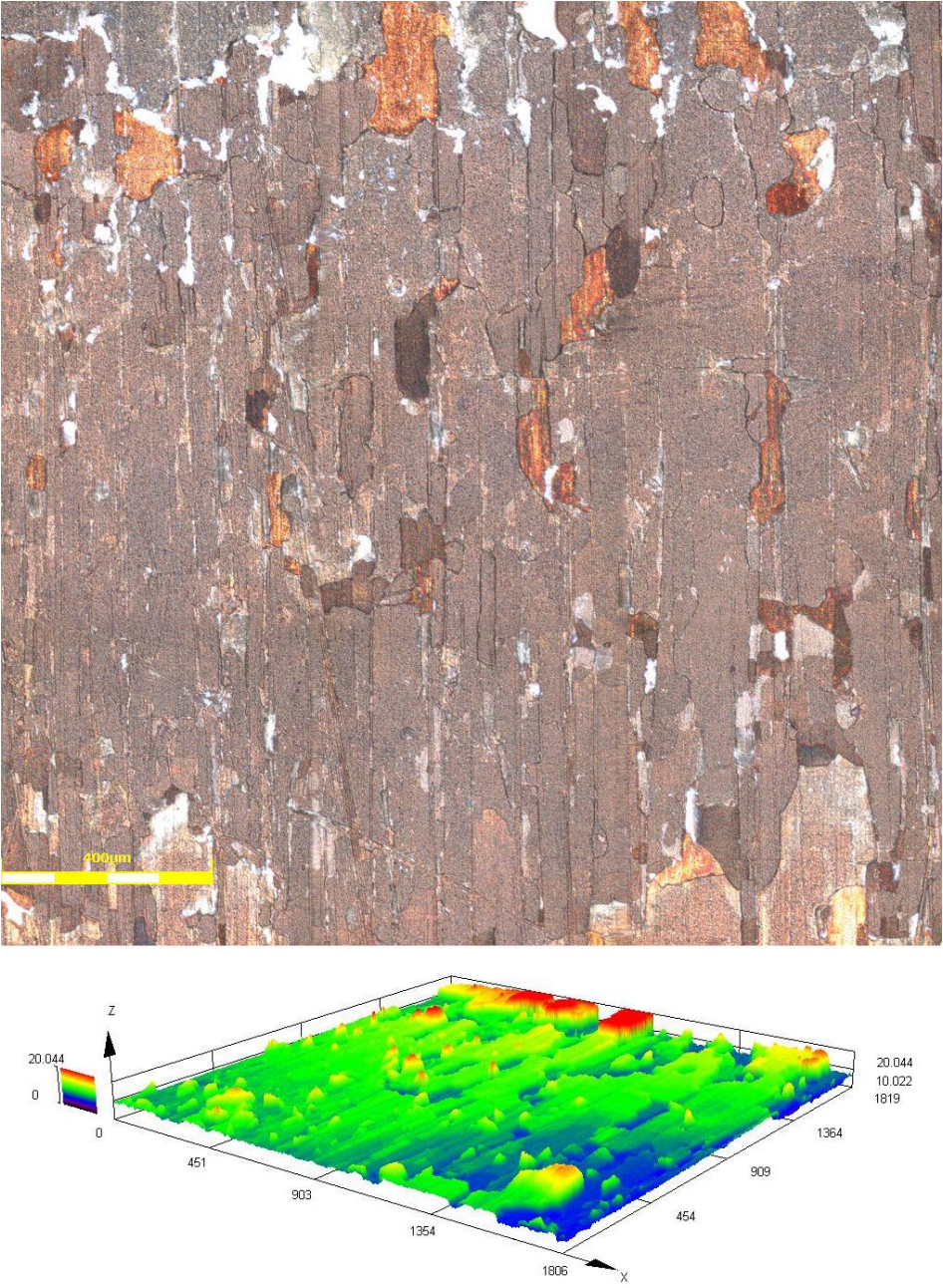
Figure 0-2: The optical microscope confocal image of surface of alumina coating on cupper at 5 mm of stand-off distance in 15 l/min with compressed air flow rate.
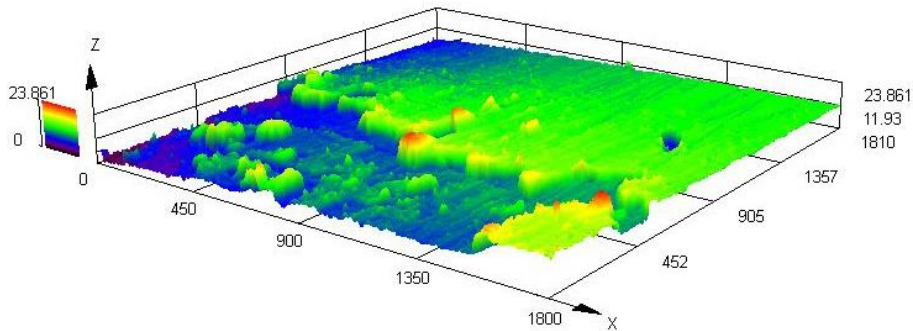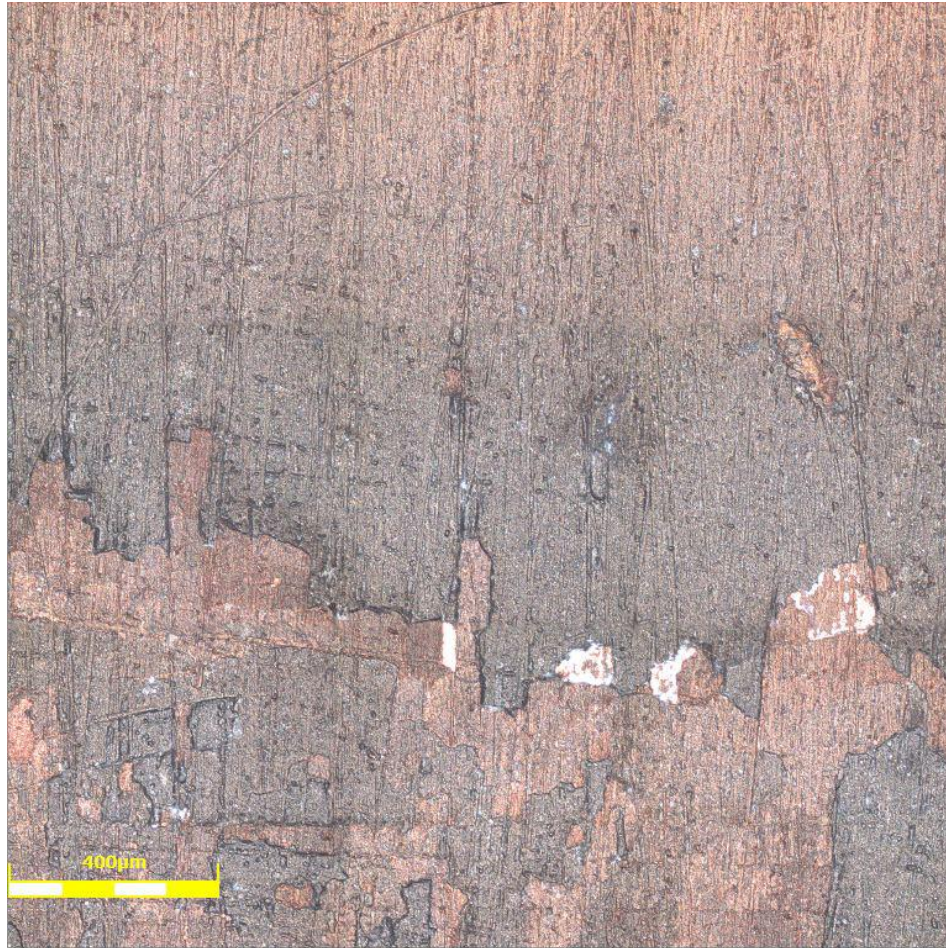
Figure 0-3: : The optical microscope confocal image of surface of alumina coating on cupper at 10 mm of stand-off distance in 15 l/min with compressed air flow rate.

The morphology of the surface coating indicated that the speed of particles is very high as well as the particle size. The efficiency of aerosol generator led to a design change which can break down the highly agglomerated particles during aerosolization and modify the vortex flow of particles inside the aerosol chamber with lower gas flow.

In the new design, a vibration table was used to create a high frequency vibration in the aerosol chamber. To modify the efficiency of fluidization, the size of the gas inlet pipe and the aerosol outlet pipe diameter was changed. These modifications improved the vortex flow of the aerosol. By increasing the frequency of the vibrator, agglomerated particles broke into a finer size and produced more appropriate fluidized particles. In addition, in the new design, the inlet gas nozzles were placed at the bottom of the chamber below the powder level so they were covered up by powders and the gas flow picked up more particles. The schematic shapes of the new aerosol generation compared to the old one are illustrated in Figure 6.4.
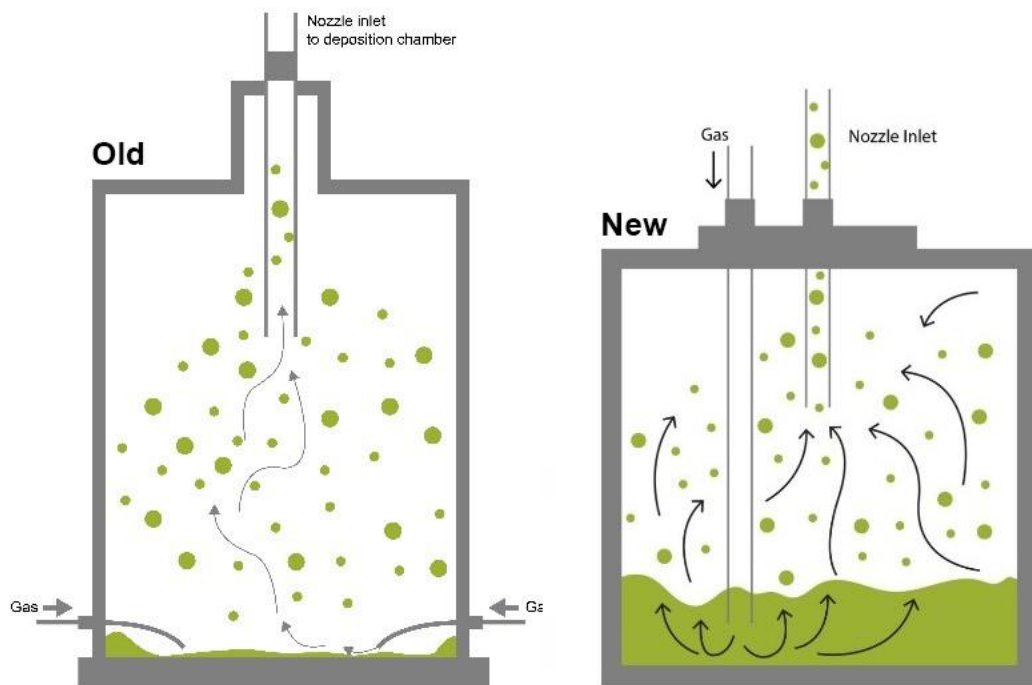
Figure 0-4: Schematic image of the new and old aerosol deposition.

The changes in new aerosol deposition provide high vortex flow at a low flow rate. This new aerosol generator with as received alumina powder in 5 l/min of compressed air and 10 mm of the stand-off distance was tested to fabricate a coating. The morphology and cross section of the coating in 4 scan passes are illustrated in Figure 6-5. The big valleys on the deposition surface and cracks inside the cross section of the deposited coating indicate that the particle impingement prevented the build up of a dense coating.
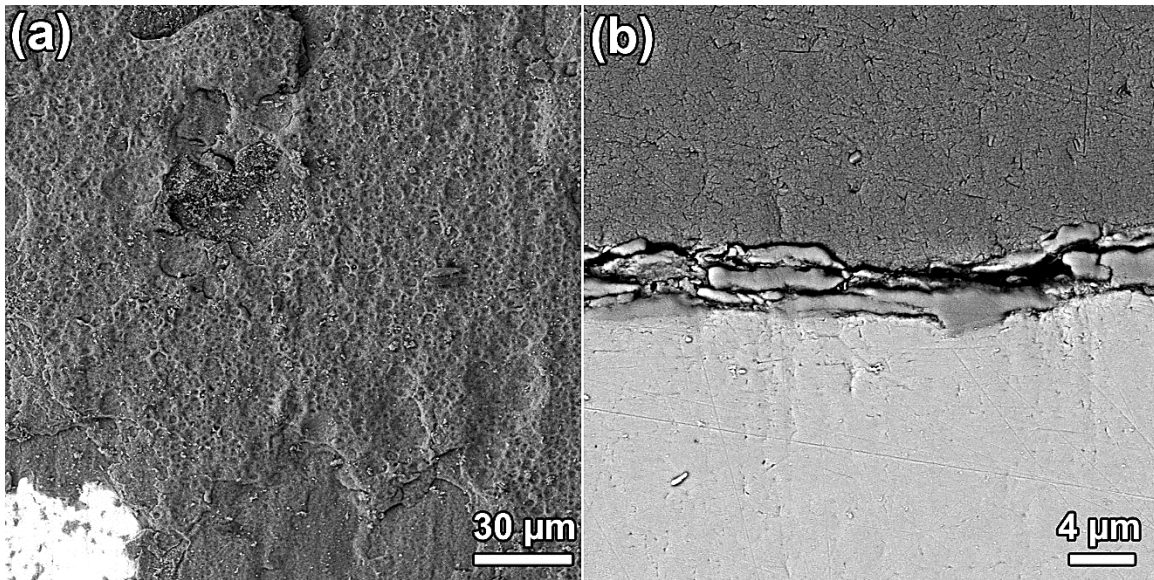
Figure 0-5: Alumina coating on steel substrate with as received powder in 10 mm of stand-off distance and 5 l/min of compressed air flow, (a) top morphology and (b) cross section of coating.

In AD process, as discussed earlier, the brittle to ductile transition (BDT) plays an effective role in fabrication of well-adhered coatings of ceramic material. To resolve this issue in alumina deposition, a ball milling process was suggested to induce more micro cracks, dislocations and modify the micro strain in the crystal structure. In this study, in order to achieve higher internal energy in the alumina particles, high energy ball milling with different milling times was used. The effect of milling process on changing the micro strain of particles shows significant improvement from as received to 4 hours milled powder. In using high energy ball milling, wet milling has been chosen since it is more efficient when compared to dry high energy ball milling. After wet milling, drying and then soft milling with polymer balls were performed. Sieving was also used to prepare particles for spraying.

The high energy milling process has been done inside of zirconia jars with alumina balls, with powder to ball ratio equals to 1:2, in the cyclohexane as wet media. The size of alumina balls was between 2- 20 mm in diameter. The wet milled powder, after high energy milling, was dried at 280 ˚C inside of the furnace, then ground and sieved with a mesh size of 75. The resulting coating, with treated powders on steel substrate and under flow of compressed air is illustrated in Figure 6-6. The peaks and deep valleys in Figure 1-6 revealed that there were still big agglomerated particles. This issue was resolved by using the N_2 gas.
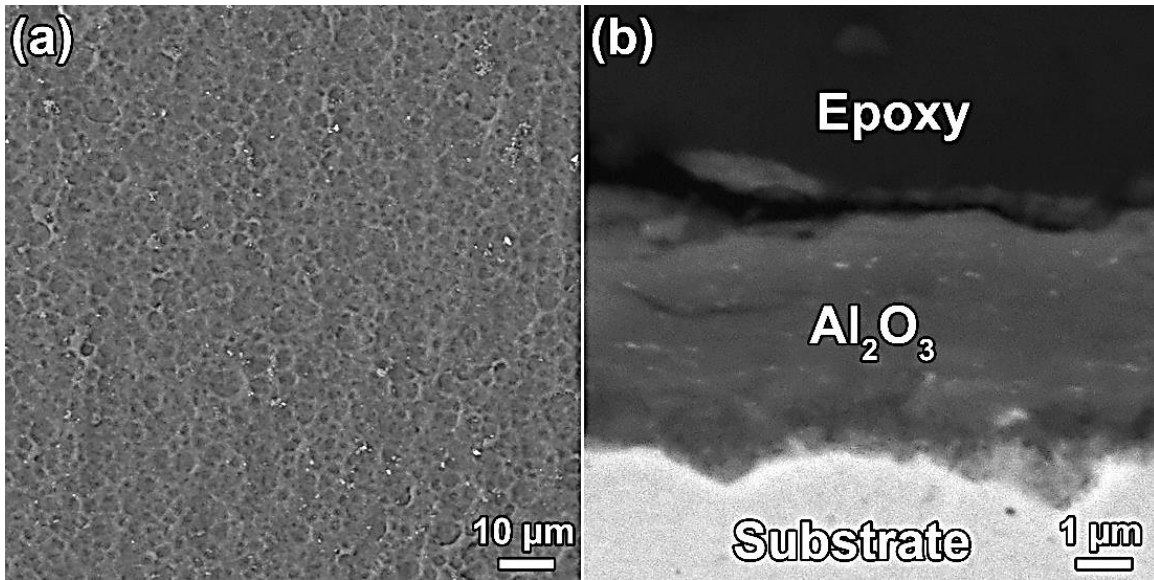
Figure 0-6: Alumina coating on steel substrate with milled powder in 10 mm of stand-off distance and with flow rate of 5 l/min, (a) top morphology and (b) cross section of coating.

N_2 gas had been suggested in AD process in some past studies. When using nitrogen, the particles stayed dryer during spraying and created finer and more uniform particles. The bottled nitrogen gas has less moisture compared to the lab compressed air supply which helps to keep the powder particles from sticking to each other in the aerosol chamber and to avoid forming agglomerated powder. Fine, dry and separated powders helped to obtain fully dense coating with good adhesion. Figure 6-7 shows the alumina coating with N_2 gas at a flow rate of 5 l/min on a stainless steel substrate.
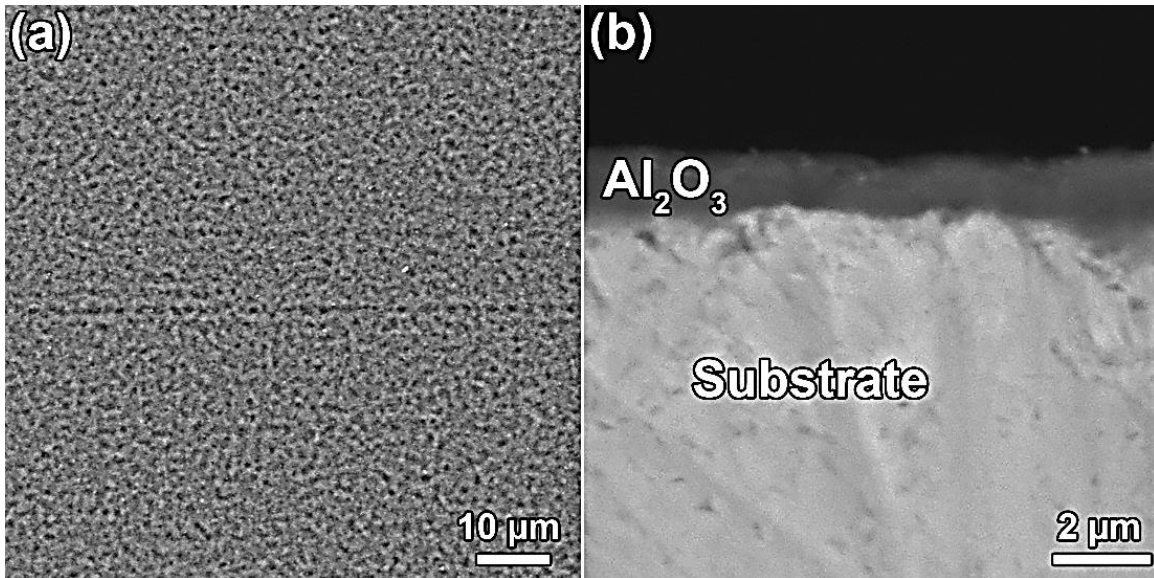
Figure 0-7: Alumina coating on steel substrate, N$_2$ carrier gas with flow rate of 5 l/min, 10 of stand-off distance, at 1 torr pressure and 4 passes.

After that, in attempts to fabricate coating on other materials, a copper substrate was tried under the new spray conditions. At a SOD distance of 5.5D$_h$, a uniform coating has been attained. The SEM images of alumina coating on copper is shown in Figure 6-8. In contrast to initial experiments, this deposition had good particle adhesion and uniformity.
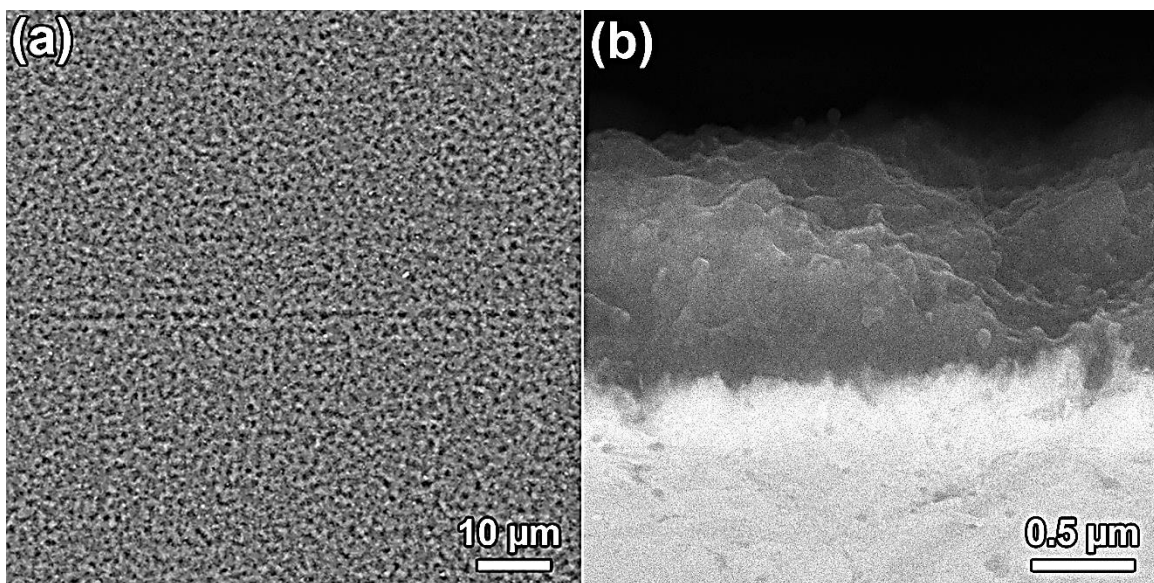
Figure 0-8: Alumina coating on copper substrate (a) top morphology and (b) cross section of deposited layers in distance of 5.5Dh.

Through the calibration and validation of the setup, operational parameters were defined and utilized in the next step of the experiment which is creating a coating of GNP-alumina. Using the milling process and under the best operation distance of 5.5Dh, and the deposition pressure of 1 torr with a flow rate of 5 l/m, four (4) passes of composite layers were deposited. More explanation and tribology results were revealed in the results chapter.

Appendix II: Numerical simulation methodology

Yeganeh et al. [70] developed the ANSYS-Fluent numerical modelling program, which was used in this study to simulate particle trajectories at two different stand-off distances. Governing equation such as; momentum, mass, energy, etc. are solved based on the finite volume method. According to the work by Yeganeh et al.[70], continuous phase is classified as a viscous flow; consequently, the Navier-Stokes equations are solved for continuous phase analysis. Because of the enormous difference in pressure between the aerosol chamber and the deposition chamber in the aerosol deposition process, the abrupt expansion of the flow after the nozzle exit is inevitable, resulting in the acceleration of the flow and the formation of a large turbulent region. Consequently, the realisable $k - \varepsilon$ turbulence model is used in this research.

For simulating the particle velocity following convergence of the solution for the continuous phase, a solution for the dispersed phase is created by infusing particles that may exchange mass, momentum, and energy with the continuous phase into the computed flow field. In this work, Lagrangian particle tracking is used to model the motion of the particles. In addition, it is assumed that particles are solid and spherical, with small volume fraction. To estimate the trajectory of a particle using the Lagrangian method, the principal active forces consist of the drag, the gravitational force and an additional acceleration force. This article[70]explains further aspects of the equation for drag coefficient, compressibility, and non-continuous parameters.

The mass flux is used for the inlet boundary condition, and the pressure within the vacuum chamber is supplied to the solver, which is set to a constant value of 1 torr for the outlet boundary condition.

The stagnation temperature in this study is also 300 K and the boundary condition for the wall of the nozzle is the isothermal with the no slip boundary condition.

To demonstrate the relationship between nozzle geometry and stand-off distance, the geometry of a converging-diverging nozzle with pressurized nitrogen gas discharging in a vacuum chamber was defined using Figure 6-9. As a result, the nozzle and its surrounding area at the exit of the nozzle inside the vacuum chamber made up the computational domain for the free-jet CFD analysis. A flat rectangular substrate with an area of 2.54× 2.54 × 0.3 cm thickness is placed at two different distances to investigate the impact of stand-off distance.

Figure 6-9 depicts the computational domain, including meshes and boundary conditions, for free jet simulation: In this analysis, the total number of quadrilateral cells for the free-jet simulation is set to 300,000, and for the stand-off distance investigation, the number of cells within the domain before the substrate is identical to the number of cells in the free-jet domain before a particular position on the substrate. The simulation results of streamline of gas flow and particle velocity in two stand-off distances were presented in chapter 4.
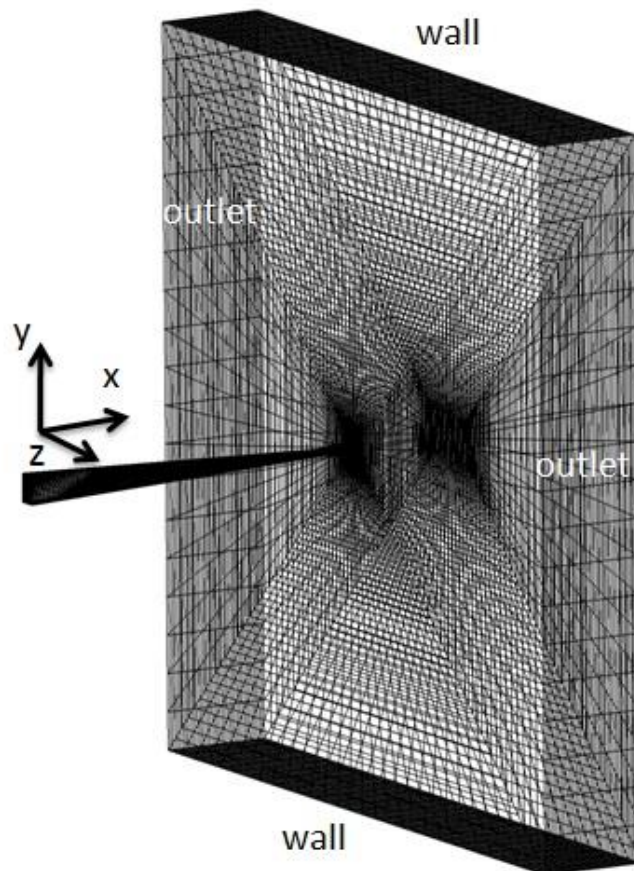

Figure 0-9: Computational domain and mesh for free jet simulation.

References

[1] E. Irissou, J.G. Legoux, A.N. Ryabinin, B. Jodoin, C. Moreau, Review on cold spray process and technology: Part I - Intellectual property, J. Therm. Spray Technol. 17 (2008) 495–516. https://doi.org/10.1007/s11666-008-9203-3.

[2] T.M. and C.H. Seiichiro Kashu1, Eiji Fuchita1, Deposition of Ultra Fine Particles Using a Gas Jet, Jpn. J. Appl. Phys. (1984).

[3] J. Akedo, M. Lebedev, Microstructure and Electrical Properties of Lead Zirconate Titanate (Pb (Zr52/Ti48) O3) Thick Films Deposited by Aerosol Deposition Method, Jpn. J. Appl. Phys. 38 (1999) 5397–5401. https://doi.org/10.1143/JJAP.38.5397.

[4] D. Hanft, J. Exner, M. Schubert, T. Stöcker, P. Fuierer, R. Moos, An overview of the Aerosol Deposition method: Process fundamentals and new trends in materials applications, J. Ceram. Sci. Technol. 6 (2015) 147–181. https://doi.org/10.4416/JCST2015-00018.

[5] J. Akedo, Room temperature impact consolidation (RTIC) of fine ceramic powder by aerosol deposition method and applications to microdevices, J. Therm. Spray Technol. 17 (2008) 181–198. https://doi.org/10.1007/s11666-008-9163-7.

[6] S. Sugimoto, V. Chan, M. Noguchi, N. Tezuka, K. Inomata, J. Akedo, Preparation of Fe/Ni-Zn-Cu ferrite stacked films by aerosol deposition method, J. Magn. Magn. Mater. 310 (2007) 2549–2551. https://doi.org/10.1016/j.jmmm.2006.11.146.

[7] O.Y. Kwon, H.J. Na, H.J. Kim, D.W. Lee, S.M. Nam, Effects of mechanical properties of polymer on ceramic-polymer composite thick films fabricated by aerosol deposition, Nanoscale Res. Lett. (2012). https://doi.org/10.1186/1556-276X-7-261.

[8] Y.H. Kim, H.J. Kim, J.H. Koh, J.G. Ha, Y.H. Yun, S.M. Nam, Fabrication of BaTiO3-PTFE composite film for embedded capacitor employing aerosol deposition, Ceram. Int. 37 (2011) 1859–1864. https://doi.org/10.1016/j.ceramint.2011.02.014.

[9] J. Exner, P. Fuierer, R. Moos, Aerosol codeposition of ceramics: Mixtures of Bi2O3-TiO2 and Bi2O3-V2O5, J. Am. Ceram. Soc. 98 (2015) 717–723. https://doi.org/10.1111/jace.13364.

[10] C.P. Jong-Jin Choi, Joo-Hoo Jang, Dong-Soo Park, Byung-Dong Hahn, Woon-Ha Yoon, Electrical Properties of Lead Zinc Niobate - Lead Zirconate Titanate Thick Films Formed by Aerosol Deposition Process, Solid State Phenom. 124–126 (2007) 169–172. https://doi.org/10.1017/CBO9781107415324.004.

[11] D.Y. Kim, B.N. Joshi, J.J. Park, J.G. Lee, Y.H. Cha, T.Y. Seong, S. In Noh, H.J. Ahn, S.S. Al-Deyabe, S.S. Yoon, Graphene-titania films by supersonic kinetic spraying for enhanced performance of dye-sensitized solar cells, Ceram. Int. 40 (2014) 11089–11097. https://doi.org/10.1016/j.ceramint.2014.03.131.

[12] Y.Y. Wang, Y. Liu, C.J. Li, G.J. Yang, J.J. Feng, K. Kusumoto, Investigation on the electrical properties of vacuum cold sprayed SiC-MoSi 2 coatings at elevated temperatures, J. Therm. Spray Technol. 20 (2011) 892–897. https://doi.org/10.1007/s11666-011-9635-z.

[13] J.J. Choi, S.H. Oh, H.S. Noh, H.R. Kim, J.W. Son, D.S. Park, J.H. Choi, J. Ryu, B.D. Hahn, W.H. Yoon, H.W. Lee, Low temperature fabrication of nano-structured porous LSM-YSZ composite cathode film by aerosol deposition, J. Alloys Compd. 509 (2011)

2627–2630. https://doi.org/10.1016/j.jallcom.2010.11.169.

[14]   J. Ryu, B.D. Hahn, J.J. Choi, W.H. Yoon, B.K. Lee, J.H. Choi, D.S. Park, Porous photocatalytic TiO2 thin films by aerosol deposition, J. Am. Ceram. Soc. 93 (2010) 55–58. https://doi.org/10.1111/j.1551-2916.2009.03391.x.

[15]   M. Schubert, C. Münch, S. Schuurman, V. Poulain, J. Kita, R. Moos, Novel method for NTC thermistor production by aerosol co-deposition and combined sintering, Sensors (Switzerland). 19 (2019) 1–11. https://doi.org/10.3390/s19071632.

[16]   M.Y. Cho, D.W. Lee, W.J. Kim, Y.N. Kim, S.M. Koo, D. Lee, K.S. Moon, J.M. Oh, Fabrication of TiO2/Cu hybrid composite films with near zero TCR and high adhesive strength via aerosol deposition, Ceram. Int. 44 (2018) 18736–18742. https://doi.org/10.1016/j.ceramint.2018.07.103.

[17]   J.H. Park, J. Akedo, M. Nakada, Surface plasmon resonance in novel nanocomposite gold/lead zirconate titanate films prepared by aerosol deposition method, Japanese J. Appl. Physics, Part 1 Regul. Pap. Short Notes Rev. Pap. 45 (2006) 7512–7515. https://doi.org/10.1143/JJAP.45.7512.

[18]   J. Akedo, Aerosol deposition of ceramic thick films at room temperature: Densification mechanism of ceramic layers, J. Am. Ceram. Soc. 89 (2006) 1834–1839. https://doi.org/10.1111/j.1551-2916.2006.01030.x.

[19]   S.H. Cho, Y.J. Yoon, H.T. Kim, J. Kim, H.J. Kim, S.M. Nam, H.K. Baik, J.H. Kim, Growth of Al 2O 3-PTFE composite film at room temperature by aerosol deposition method, Ceram. Int. 38 (2012) S131–S134. https://doi.org/10.1016/j.ceramint.2011.04.066.

[20]   J. Liu, H. Yan, K. Jiang, Mechanical properties of graphene platelet-reinforced alumina ceramic composites, Ceram. Int. (2013). https://doi.org/10.1016/j.ceramint.2013.01.041.

[21]   J. Akedo, Room temperature impact consolidation (RTIC) of fine ceramic powder by aerosol deposition method and applications to microdevices, J. Therm. Spray Technol. 17 (2008) 181–198. https://doi.org/10.1007/s11666-008-9163-7.

[22]   J. Akedo, Room temperature impact consolidation and application to ceramic coatings: Aerosol deposition method, J. Ceram. Soc. Japan. 128 (2020) 101–116. https://doi.org/10.2109/jcersj2.19196.

[23]   M.A. Piechowiak, J. Henon, O. Durand-Panteix, G. Etchegoyen, V. Coudert, P. Marchet, F. Rossignol, Growth of dense Ti3SiC2 MAX phase films elaborated at room temperature by aerosol deposition method, J. Eur. Ceram. Soc. (2014). https://doi.org/10.1016/j.jeurceramsoc.2013.11.019.

[24]   H. Bae, J. Choi, G.M. Choi, Electrical conductivity of Gd-doped ceria film fabricated by aerosol deposition method, Solid State Ionics. (2013). https://doi.org/10.1016/j.ssi.2013.01.022.

[25]   D.S. Seo, J.K. Lee, K.H. Hwang, B.D. Hahn, S.Y. Yoon, Influence of starting powders on hydroxyapatite coatings fabricated by room temperature spraying method, J. Nanosci. Nanotechnol. (2015). https://doi.org/10.1166/jnn.2015.10437.

[26]   S.Q. Fan, C.J. Li, G.J. Yang, L.Z. Zhang, J.C. Gao, Y.X. Xi, Fabrication of nano-tio 2 coating for dye-sensitized solar cell by vacuum cold spraying at room temperature, J. Therm. Spray Technol. 16 (2007) 893–897. https://doi.org/10.1007/s11666-007-9090-z.

[27]   M. Grujicic, C.. Zhao, W.. DeRosset, D. Helfritch, Adiabatic shear instability based mechanism for particles/substrate bonding in the cold-gas dynamic-spray process, Mater. Des. 25 (2004) 681–688. https://doi.org/10.1016/J.MATDES.2004.03.008.

[28]   M. Grujicic, C.. Zhao, W.. DeRosset, D. Helfritch, Adiabatic shear instability based mechanism for particles/substrate bonding in the cold-gas dynamic-spray process, Mater. Des. 25 (2004) 681–688. https://doi.org/10.1016/j.matdes.2004.03.008.

[29]   S. Kuroyanagi, K. Shinoda, A. Yumoto, J. Akedo, Size-dependent quasi Brittle–Ductile transition of single crystalline alpha-alumina particles during microcompression tests, Acta Mater. (2020). https://doi.org/10.1016/j.actamat.2020.05.065.

[30]   P. Sarobol, A.C. Hall, D.A. Urrea, M.E. Chandross, J.D. Carroll, L. Brad, W.M. Mook, P.G. Kotula, B.B. Mckenzie, D.C. Bufford, Deformation behavior of sub-micron and micron sized alumina particles in compression, (2014).

[31]   Y. Ichikawa, K. Shinoda, Current Status and Challenges for Unified Understanding of Bonding Mechanism in Solid Particle Deposition Process, (2019) 3–5.

[32]   M. Sh Migranov, S.R. Shekhtman, N.A. Suhova, A.M. Migranov, Composite nanostructured wear-resistant coatings for high-speed cutting processing, IOP Conf. Ser. Mater. Sci. Eng. 387 (2018) 012053. https://doi.org/10.1088/1757-899X/387/1/012053.

[33]   R. Rasouli, A. Barhoum, H. Uludag, A review of nanostructured surfaces and materials for dental implants: Surface coating, patterning and functionalization for improved performance, Biomater. Sci. (2018). https://doi.org/10.1039/c8bm00021b.

[34]   I. Shakhova, E. Mironov, F. Azarmi, A. Safonov, Thermo-electrical properties of the alumina coatings deposited by different thermal spraying technologies, Ceram. Int. (2017). https://doi.org/10.1016/j.ceramint.2017.08.080.

[35]   J.E. Contreras, E.A. Rodríguez, Nanostructured insulators – A review of nanotechnology concepts for outdoor ceramic insulators, Ceram. Int. (2017). https://doi.org/10.1016/j.ceramint.2017.04.105.

[36]   A.H. Pakseresht, M. Saremi, H. Omidvar, M. Alizadeh, Micro-structural study and wear resistance of thermal barrier coating reinforced by alumina whisker, Surf. Coatings Technol. (2019). https://doi.org/10.1016/j.surfcoat.2019.03.059.

[37]   T. Cygan, J. Wozniak, M. Kostecki, M. Petrus, A. Jastrzębska, W. Ziemkowska, A. Olszyna, Mechanical properties of graphene oxide reinforced alumina matrix composites, Ceram. Int. 43 (2017) 6180–6186. https://doi.org/10.1016/j.ceramint.2017.02.015.

[38]   T. He, J. Li, L. Wang, J. Zhu, W. Jiang, Preparation and Consolidation of Alumina/Graphene Composite Powders, Mater. Trans. 50 (2009) 749–751. https://doi.org/10.2320/matertrans.MRA2008458.

[39]   K. Wang, Y. Wang, Z. Fan, J. Yan, T. Wei, Preparation of graphene nanosheet/alumina composites by spark plasma sintering, Mater. Res. Bull. 46 (2011) 315–318. https://doi.org/10.1016/j.materresbull.2010.11.005.

[40]   J. Mondal, A. Marques, L. Aarik, J. Kozlova, A. Simões, V. Sammelselg, Development of a thin ceramic-graphene nanolaminate coating for corrosion protection of stainless steel, Corros. Sci. (2016). https://doi.org/10.1016/j.corsci.2016.01.013.

[41]   R. Yin, H. Wu, K. Sun, X. Li, C. Yan, W. Zhao, Z. Guo, L. Qian, Fabrication of Graphene Network in Alumina Ceramics with Adjustable Negative Permittivity by Spark Plasma Sintering, J. Phys. Chem. C. (2018). https://doi.org/10.1021/acs.jpcc.7b11177.

[42]   Q. Wang, C. Ramírez, C.S. Watts, O. Borrero-López, A.L. Ortiz, B.W. Sheldon, N.P. Padture, Fracture, fatigue, and sliding-wear behavior of nanocomposites of alumina and reduced graphene-oxide, Acta Mater. (2020). https://doi.org/10.1016/j.actamat.2019.12.035.

[43]   A. Amudha, H.D. Shashikala, O.S. Asiq Rahman, A.K. Keshri, H.S. Nagaraja, Effect of

graphene oxide loading on plasma sprayed alumina-graphene oxide composites for improved anticorrosive and hydrophobic surface, Surf. Topogr. Metrol. Prop. (2019). https://doi.org/10.1088/2051-672X/ab2707.

[44] J.W. Murray, G.A. Rance, F. Xu, T. Hussain, Alumina-graphene nanocomposite coatings fabricated by suspension high velocity oxy-fuel thermal spraying for ultra-low-wear, J. Eur. Ceram. Soc. (2018). https://doi.org/10.1016/j.jeurceramsoc.2017.10.022.

[45] L. Wang, S. Liu, J. Gou, Q. Zhang, F. Zhou, Y. Wang, R. Chu, Study on the wear resistance of graphene modified nanostructured Al2O3/TiO2 coatings, Appl. Surf. Sci. 492 (2019) 272–279. https://doi.org/10.1016/j.apsusc.2019.06.102.

[46] B. Mukherjee, O.S. Asiq Rahman, A. Islam, M. Sribalaji, A.K. Keshri, Plasma sprayed carbon nanotube and graphene nanoplatelets reinforced alumina hybrid composite coating with outstanding toughness, J. Alloys Compd. (2017). https://doi.org/10.1016/j.jallcom.2017.08.160.

[47] M. Schubert, N. Leupold, J. Exner, J. Kita, R. Moos, High-Temperature Electrical Insulation Behavior of Alumina Films Prepared at Room Temperature by Aerosol Deposition and Influence of Annealing Process and Powder Impurities, J. Therm. Spray Technol. (2018). https://doi.org/10.1007/s11666-018-0719-x.

[48] N. Seto, K. Endo, N. Sakamoto, S. Hirose, J. Akedo, Hard α-Al2O3Film Coating on Industrial Roller Using Aerosol Deposition Method, J. Therm. Spray Technol. (2014). https://doi.org/10.1007/s11666-014-0135-9.

[49] X. Wang, L. Zhang, X. Zhou, W. Wu, X. Jie, Corrosion behavior of Al2O3-reinforced graphene encapsulated Al composite coating fabricated by low pressure cold spraying, Surf. Coatings Technol. (2020). https://doi.org/10.1016/j.surfcoat.2020.125486.

[50] Y. Liu, Z. Dang, Y. Wang, J. Huang, H. Li, Hydroxyapatite/graphene-nanosheet composite coatings deposited by vacuum cold spraying for biomedical applications: Inherited nanostructures and enhanced properties, Carbon N. Y. 67 (2014) 250–259. https://doi.org/10.1016/j.carbon.2013.09.088.

[51] D.W. Lee, H.J. Kim, Y.H. Kim, Y.H. Yun, S.M. Nam, Growth process of α-Al2O3ceramic films on metal substrates fabricated at room temperature by aerosol deposition, J. Am. Ceram. Soc. 94 (2011) 3131–3138. https://doi.org/10.1111/j.1551-2916.2011.04493.x.

[52] D.W. Lee, H.J. Kim, Y.N. Kim, M.S. Jeon, S.M. Nam, Substrate hardness dependency on properties of Al 2O 3 thick films grown by aerosol deposition, Surf. Coatings Technol. (2012). https://doi.org/10.1016/j.surfcoat.2012.08.012.

[53] H.J. Kim, Y.H. Kim, J.W. Lee, S.M. Nam, Y.J. Yoon, J.H. Kim, Residual stress relief in Al 2O 3-poly-tetra-fluoro- ethylene hybrid thick films for integrated substrates using aerosol deposition, J. Nanoelectron. Optoelectron. (2012). https://doi.org/10.1166/jno.2012.1305.

[54] H.J. Kim, Y.J. Yoon, J.H. Kim, S.M. Nam, Application of Al2O3-based polyimide composite thick films to integrated substrates using aerosol deposition method, Mater. Sci. Eng. B Solid-State Mater. Adv. Technol. (2009). https://doi.org/10.1016/j.mseb.2008.12.041.

[55] S.H. Cho, Y.J. Yoon, H.T. Kim, J. Kim, H.J. Kim, S.M. Nam, H.K. Baik, J.H. Kim, Growth of Al 2O 3-PTFE composite film at room temperature by aerosol deposition method, in: Ceram. Int., 2012. https://doi.org/10.1016/j.ceramint.2011.04.066.

[56] J. Akedo, M. Ichiki, K. Kikuchi, R. Maeda, Jet molding system for realization of three-

dimensional micro-structures, Sensors Actuators A Phys. 69 (1998) 106–112. https://doi.org/10.1016/S0924-4247(98)00059-4.

[57] A. C1624-05 (2015), Standard Test Method for Adhesion Strength and Mechanical Failure Modes of, ASTM Int. C1624-05 (2012) 1–29. https://doi.org/10.1520/C1624-05R15.Scope.

[58] J. Exner, M. Hahn, M. Schubert, D. Hanft, P. Fuierer, R. Moos, Powder requirements for aerosol deposition of alumina films, Adv. Powder Technol. 26 (2015) 1143–1151. https://doi.org/10.1016/j.apt.2015.05.016.

[59] Y. Xie, H. Li, C. Ding, X. Zheng, K. Li, Effects of graphene plates' adoption on the microstructure, mechanical properties, and in vivo biocompatibility of calcium silicate coating, Int. J. Nanomedicine. 10 (2015) 3855–3863. https://doi.org/10.2147/IJN.S77919.

[60] A.C. Ferrari, Raman spectroscopy of graphene and graphite: Disorder, electron-phonon coupling, doping and nonadiabatic effects, Solid State Commun. (2007). https://doi.org/10.1016/j.ssc.2007.03.052.

[61] M.S. Dresselhaus, A. Jorio, M. Hofmann, G. Dresselhaus, R. Saito, Perspectives on carbon nanotubes and graphene Raman spectroscopy, Nano Lett. 10 (2010) 751–758. https://doi.org/10.1021/nl904286r.

[62] K. Chu, C. Jia, Enhanced strength in bulk graphene-copper composites, Phys. Status Solidi. 211 (2014) 184–190. https://doi.org/10.1002/pssa.201330051.

[63] D. Zhang, Z. Zhan, Strengthening effect of graphene derivatives in copper matrix composites, J. Alloys Compd. 654 (2016) 226–233. https://doi.org/10.1016/j.jallcom.2015.09.013.

[64] X. Gao, H. Yue, E. Guo, H. Zhang, X. Lin, L. Yao, B. Wang, Mechanical properties and thermal conductivity of graphene reinforced copper matrix composites, Powder Technol. 301 (2016) 601–607. https://doi.org/10.1016/j.powtec.2016.06.045.

[65] D.-W. Lee, H.-J. Kim, Y.-N. Kim, M.-S. Jeon, S.-M. Nam, Substrate hardness dependency on properties of Al2O3 thick films grown by aerosol deposition, Surf. Coatings Technol. 209 (2012) 160–168. https://doi.org/10.1016/j.surfcoat.2012.08.012.

[66] C. Zhang, A. Nieto, A. Agarwal, Ultrathin graphene tribofilm formation during wear of Al 2 O 3 –graphene composites, Nanomater. Energy. 5 (2016) 1–9. https://doi.org/10.1680/jnaen.15.00027.

[67] D. Berman, A. Erdemir, A. V. Sumant, Few layer graphene to reduce wear and friction on sliding steel surfaces, Carbon N. Y. 54 (2013) 454–459. https://doi.org/10.1016/j.carbon.2012.11.061.

[68] H. Liang, Y. Bu, J. Zhang, Z. Cao, A. Liang, Graphene Oxide Film as Solid Lubricant, ACS Appl. Mater. Interfaces. 5 (2013) 6369–6375. https://doi.org/10.1021/am401495y.

[69] J. Li, J. Li, J. Luo, Superlubricity of Graphite Sliding against Graphene Nanoflake under Ultrahigh Contact Pressure, Adv. Sci. 5 (2018) 1800810. https://doi.org/10.1002/advs.201800810.

[70] A.Z. Yeganeh, M. Jadidi, C. Moreau, A. Dolatabadi, Numerical Modeling of Aerosol Deposition Process CR, Surf. Coat. Technol. (2019). https://doi.org/10.1016/j.surfcoat.2019.04.094.